Native copper formation associated with serpentinization in the Cheshmeh-Bid ophiolite massif (Southern Iran)

Alireza Eslami, Benjamin Malvoisin, Giovanni Grieco, László Előd Aradi, Claudio Marchesi, Alessandro Cavallo, Alessandra Montanini, Giulio Borghini, Ryan Mathur, Kei Ikehata, et al.

Native copper formation associated with serpentinization in the Cheshmeh-Bid ophiolite massif (Southern Iran)

Alireza Eslami[1*], Benjamin Malvoisin[1], Giovanni Grieco[2], László Előd Aradi[3], Claudio Marchesi[4,5], Alessandro Cavallo[6], Alessandra Montanini[7], Giulio Borghini[2], Ryan Mathur[8], Kei Ikehata[9], Donald W. Davis[10], Chun-Hui Li[11], Csaba Szabó[3]

[1]ISTerre, Univ. Grenoble Alpes, Univ. Savoie Mont Blanc, CNRS, IRD, IFSTTAR, 38041 Grenoble, France

E-mail: alireza.eslami@univ-grenoble-alpes.fr

[2]Dipartimento di Scienze della Terra, Università degli Studi di Milano, Via Botticelli 23, I-20133 Milano, Italy

[3]Lithosphere Fluid Research Lab, Eötvös Loránd University, Pázmány Péter sétány 1/C, Budapest H-1117, Hungary

[4]Departamento de Mineralogía y Petrología, Universidad de Granada, Avenida Fuentenueva s/n, 18002, Granada, Spain

[5]Instituto Andaluz de Ciencias de la Tierra, CSIC-Universidad de Granada, Avenida de las Palmeras 4, 18100 Armilla, Granada, Spain

[6]Università degli Studi di Milano-Bicocca, Milano, Italy

[7]DIFEST, Università di Parma, Parco Area delle Scienze 157a, 43100 Parma, Italy

[8]Department of Geology, Juniata College, Huntingdon, Pennsylvania 16652, USA

[9]Faculty of Life and Environmental Sciences, University of Tsukuba, 1-1-1 Tennodai, Tsukuba, Ibaraki, 305-8577, Japan

[10]Department of Earth Sciences, University of Toronto, Ontario M5S 3B1, Canada

[11]CAS Key Laboratory of Crust–Mantle Materials and Environments, School of Earth and Space Sciences, University of Science and Technology of China, Hefei, 230026 Anhui, China

Abstract

In the Cheshmeh-Bid district of the Khajeh-Jamali ophiolitic massifs (Southern Iran), mantle peridotites are intruded by abundant pyroxenite dykes. A few of these dykes are remarkable for the occurrence of native copper associated with the development of a metasomatic reaction zone. The dykes are progressively reacted, from their margins towards the center, with an amphibole + antigorite selvage, followed by a centimeter-thick clinopyroxene + antigorite assemblage and, finally, by the native copper-bearing zone consisting of clinopyroxene + chlorite + antigorite. Native Cu occurs along cleavages and partially healed fractures in clinopyroxene, and as massive grains intergrown with antigorite. Copper isotope signatures and thermodynamic calculations show that the main driver for reaction zone formation is Ca-metasomatism. Native copper forms at the expense of chalcocite in the reaction zone. Such a reaction can only occur in reducing conditions, in agreement with the analysis of fluid inclusions composition displaying H_2 and CH_4. Such fluids presumably originated from the hydration of mantle rocks. The observed reaction zone and native copper mineralization are thus interpreted as the result of Ca-metasomatism during hydrothermal alteration of the oceanic lithosphere. This is consistent with U/Pb dating of titanite, suggesting formation during the Albian when the dykes were exposed on the seafloor in a supra-subduction setting. The source for copper mineralization, as revealed by Cu isotopes, is probably mantle-like.

Keywords: Native copper; serpentinization; Ca-metasomatism; pyroxenite; Cheshmeh-Bid ophiolitic massif; Iran

1. Introduction

Native copper has been documented in ultramafic and mafic rocks from ophiolitic and orogenic massifs. It was observed in partially serpentinized peridotites of Costa Rica (Schwarzenbach

et al., 2014), pillow basalts from la Désirade, Lesser Antilles island arc (Nagle et al., 1973), rodingitized gabbro in serpentinites of the Braszowice-Brzeznica Massif, Poland (Gunia, 1986), basal cumulate sequence of the massif from the Zambales ophiolite, Philippines (Abrajano and Pasteris, 1989), plagioclase lherzolites from the Horoman peridotite complex, Hokkaido, northern Japan (Ikehata and Hirata, 2012) and websterite from the Totalp ultramafic massif, Swiss Alps (Van Acken et al., 2007). Three hypotheses have been put forward to explain the genesis of native copper in peridotites and basalts: ((i) crystallization in equilibrium with a mafic magma (e.g. Cabral and Beaudoin, 2007; Ikehata and Hirata, 2012); (ii) low-temperature in situ alteration of magmatic or hydrothermal Cu-sulfides at highly reducing conditions (e.g. Lorand and Grégoire, 2006; Schwarzenbach et al., 2014); (iii) precipitation from low-temperature hydrothermal fluids (e.g. Dekov et al., 2013; Ikehata et al., 2016).

Thermodynamic calculations show that hypothesis (ii) requires reducing conditions for native copper to precipitate in hydrothermal environments (Schwarzenbach et al., 2014). The observation of Fe-Ni alloys and native metals in serpentinized peridotites (e.g. Klein and Bach, 2009; Schwarzenbach et al., 2014) shows that highly reducing conditions prevail during serpentinization. This is consistent with vent fluid compositions measured in ultramafic-hosted hydrothermal fields (Charlou et al., 2002) and gas seep compositions analyzed in ophiolites (e.g. Abrajano et al., 1988). During serpentinization, hydrogen production relates to water reduction coupled with iron oxidation during replacement of primary olivine and pyroxene by secondary magnetite and serpentine (McCollom and Bach, 2009; Malvoisin et al., 2012). Water-rock interaction is also intimately associated with Ca-metasomatism of mafic rocks in which the removal of silica (SiO_2) and addition of Ca are the main mass transfers (Coleman 1967).

In this contribution, we report a new occurrence of native copper mineralization within Ca-metasomatically altered pyroxenites from the Cheshmeh-Bid ophiolitic massif in the Khajeh-

77 Jamali area, Southern Iran. Based on field and petrographic observations combined with new
78 geochronological and geochemical data we aim to: (1) define the paragenetic sequence of the
79 ore and silicate minerals; (2) produce a thermodynamic model for the origin of Ca-
80 metasomatism and native copper; (3) determine the sources of Cu in the mineralization system;
81 (4) constrain the timing of the copper mineralization and, finally, (5) develop a conceptual
82 model of native copper genesis within metasomatised pyroxenite veins.
83

84 ## 2. Geological setting

85 The Iranian Ophiolites (Fig. 1a) represent the remnants of the Tethyan oceanic lithosphere in
86 the Anatolian segment of the Alpine–Himalayan Orogen. Mesozoic ophiolites of Iran have
87 been divided into five ophiolitic belts (Shafaii Moghadam and Stern, 2015): (1) Late
88 Cretaceous Zagros Outer Belt (ZOB) ophiolites along the Main Zagros Thrust including
89 Kermanshah-Kurdistan, Maku-Khoy-Salmas, Neyriz/Khajeh-Jamali and Haji Abad ophiolites;
90 (2) Late Cretaceous Zagros Inner Belt (ZIB) ophiolites including Nain, Dehshir, Shahr-e-Babak
91 and Balvard-Baft ophiolites along the main boundaries of the Central Iranian Micro-
92 continental block; (3) Late Cretaceous-Early Paleocene Sabzevar-Torbate-Heydarieh
93 ophiolites in the northeast of Iran; (4) Early to Late Cretaceous ophiolites including
94 Nehbandan, Birjand and Tchehel-Kureh ophiolites between the Afghan and Lut blocks; and
95 (5) Late Jurassic-Cretaceous Makran ophiolites in the southeast of Iran. The Khajeh-Jamali
96 ophiolites consist of four ophiolitic massifs belonging to ZOB in the Zagros Mountains
97 (Southwestern Iran), and outcrop about 20 km from the Main Zagros Thrust (Fig. 1a). These
98 massifs are dominantly composed of mantle harzburgite-dunite tectonites and a Moho
99 Transition Zone (MTZ) (Fig. 1b; e.g. Rajabzadeh, 1998; Rajabzadeh and Nazari Dehkordi,
100 2013; Eslami et al., 2015). Several concordant or subconcordant orthopyroxenites and
101 clinopyroxenites intrude both mantle tectonites and the MTZ. Boundaries between the

pyroxenite intrusions and peridotite host rocks are generally sharp. The pyroxenite dykes/veins are usually coarse-grained and range from a few cm to 35 cm in thickness.

A typical cumulate sequence and a sheeted dyke complex are missing in the Khajeh-Jamali area. Peridotites are overlain by a very thin nappe of basaltic pillow lavas, reddish-purple radiolarian cherts and Late Cretaceous pelagic limestones (Rajabzadeh, 1998; Eslami et al., 2015). The ophiolitic assemblage is thrust onto the Cenomanian/Turonian shallow water deposits of the Sarvak Formation in the western portion of the Khajeh-Jamali area (Alavi, 1994). The Cheshmeh-Bid ophiolitic massif covers rugged mountainous area of ~25 km^2 in the northwest of the Khajeh-Jamali area. This massif hosts large economical concentrations of chromitites showing massive and high-grade disseminated texture (Rajabzadeh, 1998; Eslami et al., 2015). In the Cheshmeh-Bid chromitite mine, a few pyroxenite dykes and veins crosscutting massive chromitite and serpentinized dunite are partially (Fig. 2a, b) or completely (Fig. 2c) metasomatised with remarkable native copper mineralization.

3. Analytical methods

Analytical work has been focused on five representative samples of metasomatically altered pyroxenite veins (KJPX04, KJPX05, KJPX06, KJPX11 and KJPX12) and two fresh pyroxenites (KJPX01 and KJPX20). Polished thin sections of both fresh and altered pyroxenites were examined under transmitted light using a Leica optical microscope at University of Milan. Samples KJPX04, KJPX05 and KJPX06 were selected for petrography observation because they show typical metasomatic zoning on the micrometer scale.

3.1 Major and trace element analyses in minerals and whole-rocks

Quantitative chemical analyses of silicate minerals (except chlorite) were obtained using a JEOL JXA-8230 electron probe micro-analyzer (EPMA) equipped with five wavelength-

dispersive spectrometers (WDS) at the Institut des Sciences de la Terre, Université Grenoble Alpes, France. Analytical conditions were: 15 kV acceleration voltage, 12nA beam current, 3μm beam size. Natural minerals, pure metal and synthetic oxides were used as standards and ZAF correction was applied. Spectral interference (V Kα vs Ti kβ) was corrected using the software-calculated correction factor. Elemental distribution maps were done at an accelerating voltage of 15kV, a beam current of 100 nA and a dwell time of 200 ms. Major element composition of chlorites, sulfides and spinels were analyzed using a JEOL JXA 8200 Superprobe equipped with five wavelength-dispersive (WDS) spectrometers, an energy dispersive (EDS) spectrometer, and a cathodoluminescence detector (accelerating potential 15 kV, beam current 15 nA), at the Dipartimento di Scienze della Terra "Ardito Desio", University of Milano (Italy).

Major elements and Cr and Ni in whole-rock samples were analysed by X-ray Fluorescence (XRF) with a BRUKER S4-Pioneer instrument at the Instituto Andaluz de Ciencias de la Tierra (IACT, Granada, Spain), using standard sample preparation and analytical procedures. The accuracy of analyses was assessed by repeated analyses of international reference material JP-1 (peridotite) handled as unknown, which show good agreement with accepted values for this standard (Govindaraju, 1994). Whole-rock trace elements (REE, Ba, Th, Pb, Nb, Ta, Sr, Y and Sc) were analyzed by an Agilent 8800 QQQ ICP–MS (Inductively Coupled Plasma–Mass Spectrometer) at the IACT. Sample digestion was performed following the $HF/HClO_4$ dissolution procedure described in detail by Ionov et al. (1992), and element concentrations were determined by external calibration using aqueous solutions. Accuracy of the ICP–MS analyses has been assessed analyzing the BIR-1 basalt standard as an unknown, which show good agreement with reference concentrations of Jochum et al. (2016).

3.2 Copper isotope analyss

Grains of native copper were separated through crushing and hand picking. Samples were processed similar to the techniques in previous studies, namely Bornhorst and Mathur (2017), Mathur et al. (2009a) and Wall et al. (2011). The native copper samples were dissolved in Teflon beakers with 8 mL of ultrapure aquaregia at 140°C for 24 hours or until complete dissolution occurred. Samples were diluted to 100 ng/g for Cu isotope analysis with a Neptune MC-ICP-MS at Pennsylvania State University. Copper isotope compositions are reported in the traditional per mil format compared to the NIST 976 international standard. Mass bias was corrected for using standard-sample-standard bracketing. All samples matched the intensities of the standards within 25 %. An internal copper metal standard (USA 1838 Cent, reported in Mathur et al. 2009b) was measured 4 times during the session and produced a $d^{65}Cu$= 0.04+/- 0.05 per mil value. This value is identical to accepted δ65Cu of the standard (-0.02 per mil +\- 0.08).

3.3 U-Pb LA-ICP-MS analysis of titanite

Titanite grains were ablated in thin section using a 213 nm laser beam with diameter of 25 μm at 5 Hz and 40 % power (NWA ablation system). ICP-MS analyses were carried out using a Plasmaquad instrument. Data were collected on ^{206}Pb, ^{207}Pb, and ^{238}U. Immediately prior to each analysis, the spot was briefly pre-ablated over a larger area than the beam diameter to clean the surface. Following a 10 s period of baseline accumulation the laser sampling beam was turned on and data were collected for 25 s followed by a 50 s washout period. About 150 measurement cycles per sample were produced and ablation pits are about 15 μm deep. Data were edited and reduced using custom VBA software (UTILLAZ program) written by the author. $^{206}Pb/^{238}U$ show only slight fractionation caused by hole depth through the run and most of the $^{207}Pb/^{206}Pb$ and $^{206}Pb/^{238}U$ data can be averaged. Pb-204 was not measured since this peak is relatively small and would require a large amount of measurement time as well as being

subject to interference from ^{204}Hg in the Ar. Ages are determined by projecting data along a common Pb mixing line to the concordia curve (see Results below). Titanite from a quartz diorite sample in northwest Ontario, DD81-29, previously dated at 2700 ± 2 Ma (Davis and Edwards, 1986) was used as a standard.

3.4 Raman Spectroscopy

Raman spectroscopic analyses were carried out at the Research and Industrial Relations Center of the Faculty of Science at the Eötvös University, Budapest. Analyses were carried out with a Horiba LabRAM HR800 spectrometer, using a 532 nm (green) laser with a maximum laser energy of 130 mW (~25 mW on the sample surface). A 100 μm confocal pinhole and an optical grating with 1800 grooves/mm were used. The spectral resolution of the measurements was 0.8 cm^{-1} at 1707.9 cm^{-1} (defined as the measured full width at half maximum values of neon atomic emission lines). During the measurements an objective with 100× magnification was used (NA=0.9). Analyses ran with 2 to 5 repetitions for an accumulated 200-500 seconds.

3.5 Thermodynamic modelling

We used thermodynamic modelling to determine (1) the conditions prevailing during native copper formation, and (2) the factors controlling metasomatism. The calculations were performed differently for these two objectives. We therefore constructed phase diagrams in the Fe-Ni-Cu-O-S system with SUPCRT92 (Johnson et al., 1992) for (1). We used the thermodynamic database provided in Klein and Bach (2009) in which the SUPCRT92 database is extended by including thermodynamic data for Fe-Ni sulfides. The diagrams are computed as a function of the activities of $H_{2,aq}$ ($aH_{2,aq}$) and $H_2S_{,aq}$ ($aH_2S_{,aq}$) at aH_2O = 1 and 50 MPa. This latter pressure is used to compute equilibrium constants in Klein and Bach (2009), and is relevant for serpentinization on the seafloor.

We used Gibbs energy minimization with Perple_X (Connolly, 2005) for (2) because it provides solid solutions for the phases observed here. This ensures accurate modelling of the distribution of major elements during metasomatism. The equilibrium assemblages were determined for the composition of the orthopyroxenite (sample IRKJPX20; Supplementary Table 10) as a function of the chemical potential of CaO and temperature at 50 MPa. We did not include components with a concentration below 0.5 wt.% in the calculation. The chemical potential of CaO was also computed as a function of temperature for three metasomatised samples (IRKJPX04, IRKJPX11 and IRKJPX12). We used the thermodynamic database of Holland and Powell (1998a) and the solid solution models of Holland and Powell (1996) for orthopyroxene and clinopyroxene, Holland and Powell (1998a) for olivine, spinel and staurolite, Holland and Powell (1998b) for chlorite, Diener et al. (2007) for amphibole, Padrón-Navarta et al. (2013) for antigorite and White et al. (2000) for garnet. The solid solutions for talc and brucite were considered as ideal. H_2O was added in excess and modelled with the CORK equation of state (Holland and Powell, 1998). This explains why the orthopyroxenite is not composed of orthopyroxene in the calculations but rather of its hydration products (talc and antigorite). We did not consider here the kinetic effects that led to orthopyroxene preservation. Copper, and iron-nickel sulfides are not all available in Perple_X. We therefore constructed phase diagrams in the Fe-Ni-Cu-O-S system with SUPCRT92 (Johnson et al., 1992) for (2). We used the thermodynamic database provided in Klein and Bach (2009) at 50 MPa in which the SUPCRT92 database is extended by including thermodynamic data for Fe-Ni sulfides. The diagrams are computed as a function of the activities in $H_{2,aq}$ ($a_{H2,aq}$) and $H_2S_{,aq}$ ($a_{H2S,aq}$) at a_{H2O} = 1 and at the pressure at which the thermodynamic data are available (50 MPa).

4 Results

4.1 Petrography of the host peridotites

Petrography of the Cheshmeh-Bid host peridotites and chromitites has been discussed in detail by previous authors (e.g. Rajabzadeh, 1998; Eslami, 2015). The scarcity of bastite suggests that the host peridotites of the studied pyroxenites was originally a dunite. The host dunites consist of >95 % mesh-textured serpentine, cut by serpentine veins, plus 1—3 % spinel minerals. The Cheshmeh-Bid harzburgites are composed of 70-85 modal% olivine and 10-20 modal% orthopyroxene. The minor phases are fine-grained anhedral clinopyroxene (3–5 modal%) and subhedral spinel (0.5–3 modal%). Pervasive alteration in harzburgite includes the formation of serpentine minerals after olivine and orthopyroxene. In the Cheshmeh-Bid peridotites, Fe, Cu and Ni commonly form fine-grained opaque minerals including oxides (magnetite), sulfides (pentlandite, heazlwoodite) and alloys (awaruite) that occur together with (accessory) platinum-group minerals (PGM). Base metal sulfide inclusions inside alloys show desulfurization effects in the matrix of the Cheshmeh-Bid chromitite and host dunite and harzburgite (Eslami, 2015).

4.2 Petrography and mineral chemistry of pyroxenite and reaction zones in contact with host peridotites

Along the interface with the peridotite host rock, orthopyroxenite veins developed three mineralogically and chemically distinct alteration zones. These are described below. The transition between least altered and altered zones can either be sharp or progressive.

4.2.1. Orthopyroxenite. The least altered mineral assemblage of the pyroxenite vein comprises orthopyroxenea and chromian spinel. It occurs in a zone with an average thickness of 1.5 cm (hereafter Opx-rich zone; Fig. 3a). Clinopyroxene, olivine and antigorite are secondary minerals in this zone. This zone displays a porphyroclastic texture with 1 to 3 mm large pyroxene grains surrounded by antigorite. The composition of orthopyroxene in this zone is mostly enstatitic (Supplementary Fig.1), with Mg# [$Mg/(Mg+Fe_{tot})$] of 0.90–0.93.

Orthopyroxene has Cr_2O_3, Al_2O_3 and TiO_2 contents of 0.12–0.46 wt.%, 0.40–1.38 wt.% and <0.05 wt.%, respectively (Supplementary Table S1). The orthopyroxene crystals contain numerous ovoid and lamellar exolutions of clinopyroxene (Fig. 3b). Clinopyroxene exolutions in the Opx-rich zone have high CaO contents ranging between 21.02– 23.62 wt.% (with average of 22.94 wt.%), low Al_2O_3 contents of 0.50-2.20 wt.% (with average of 1.33 wt.%) and Cr_2O_3 contents of 0.26 to 0.94 wt.% with average of 0.63 wt.% (Supplementary Table S2). The Mg# of clinopyroxene exolutions, observed in large orthopyroxenes, range from 0.91 to 0.99. Clinopyroxene from pyroxenites are mostly diopside (Supplementary Fig. 1).

In Opx-rich zone of Cu-rich pyroxenites, secondary olivine occurred as vein-like texture in the middle of antigorite around the orthopyroxene porphyroclasts (Fig. 3c). Representative analyses of olivine with vein-like texture from the Cu-bearing pyroxenites are given in Supplementary Table S3. Olivine has low forsterite contents comprised between 75 and 83 mol.%. Compared to the vein-like textured olivine in Cu-bearing pyroxenites, primary olivines found in dunite and harzburgite of the studied area have considerably higher Fo content (91-95 mol %) (Fig. 4; Rajabzadeh and Nazari-Dehkordi, 2013). MnO contents for vein-like textured olivines vary from 0.34 to 0.82 wt.% whereas they are lower than 0.21 wt.% for olivine in associated harzburgite and dunite (Fig. 4a). NiO contents for vein-like textured olivines are homogeneous in all samples and lower (0.08 to 0.16 wt.%) compared to those in associated dunite and harzburgite (0.27-0.66 wt.%) (Fig. 4b). MnO contents and Mg# are negatively correlated for vein-like textured olivines whereas there is a broad positive correlation between NiO contents and Mg# for olivines from associated harzburgite and dunites.

Euhedral or subhedral chromian spinel (50 μm to 2.5 mm in diameter) is interstitial or included in orthopyroxene grains (Fig. 3d). Chromian spinel grains show alteration to ferrian chromite across their cracks and fractures. Rarely, spongy reaction rims developed around homogeneous chromian spinel grains. Sieve-textured rims of chromian spinel results from the occurrence of

277 several euhedral to anhedral inclusions of chlorite and clinopyroxenes (Fig. 3e). Inclusion sizes
278 range from 5 to 100 μm. Fresh cores of spinel show Cr# [Cr/(Cr + Al)] ranging from 0.65 to
279 0.73 (average of 0.70) and Mg# [Mg/(Mg + Fe^{2+})] from 0.49 to 0.59 (average of 0.55)
280 (Supplementary Table S4; Fig. 5). These high-Cr# spinels are characterized by low TiO_2
281 content < 0.18 wt.%, MnO contents of 0.04-0.24 wt.%, FeO contents of 18.29-25.21 wt.%,
282 Al_2O_3 contents of 13.38–20.29 wt.% (Fig. 5).
283 The products of three successive reactions overprinted the Opx-rich zone. We distinguished
284 three reaction zones from inner to outer portions of the orthopyroxenite dykes:
285 *4.2.2. Zone I* is characterized by a narrow selvage of amphibole with subordinate antigorite
286 between Opx-rich zone and Zone II. The thickness of this zone is 50 μm to 100 μm (Fig. 3a).
287 The chemical composition of amphibole from the Cheshmeh-Bid pyroxenites is given in
288 Supplementary Table S5. Based on the nomenclature of Leake et al. (1997), amphiboles show
289 a wide range of compositions from tremolite to magnesio-hornblende and edenite. They are
290 characterized by Mg# between 0.92 and 0.98, TiO_2 <0.07 wt.%, Cr_2O_3 contents are between
291 0.12 and 2.50 wt.% and Al_2O_3 contents between 0.26-10.30 wt.%.
292 *4.2.3. Zone II* is composed of clinopyroxene megacrysts with subordinate antigorite and very
293 rare orthopyroxene. The thickness of this zone is from 1 cm to 1.5 cm (Fig. 3a). Clinopyroxenes
294 in Zone II show a wide range of Mg# (0.75-0.98) and are characterized by CaO contents of
295 21.95– 26.1 wt.% with average of 23.25 wt.%, Al_2O_3 and Cr_2O_3 contents lower than 2.23 wt.%
296 and 1.56 wt.%, respectively (Supplementary Table S2; Supplementary Fig. 1). Light grey bands
297 on zoned clinopyroxenes in Zone II have lower Mg# values (0.76-0.80) and higher Cr_2O_3
298 contents compared to dark grey zones (Fig. 3f). Sporadic inclusions of amphiboles are
299 discernible along the cleavage of clinopyroxenes (Fig. 3g). Amphibole inclusions in Zone II
300 are magnesio-hornblende to edenite. They are characterized by Mg# between 0.90 and 0.97
301 and TiO_2 contents <0.23 wt.%, Cr_2O_3 contents of 0.80-2.53 wt.% and Al_2O_3 contents of 4.14-

9.71 wt.% (Supplementary Table S5). Orthopyroxene inclusions in diopside megacrysts of Zone II show lower Mg# (~ 0.87). These inclusions have average Al_2O_3 = 1.5 wt.% and Cr_2O_3 = 0.51 wt.%. Clinopyroxene is locally replaced by calcite with perfect rhombohedral cleavage (Fig. 3h, 3i).

4.2.4. Zone III is the mineralized zone consisting dominantly of clinopyroxene, chlorite, antigorite and native copper. Zone III range from 0.5 cm to 1.5 cm in width and is typically massive in texture (Fig. 3a). Antigorite forms well-shaped tablets or laths that penetrate deeply into the clinopyroxenes. Chlorite forms patches or more commonly occurs interstitially in between the antigorite plates (Fig. 3j). It shows chemical variations (dominantly clinochlore) in each set of samples (Supplementary Table S6). Generally, chlorites in Zone III from the studied pyroxenites display low FeO (<5.08 wt.%), high MgO (28.46-33.26 wt.%) and variable Cr_2O_3 contents (0.17-3.84 wt.%). Chlorites are mainly clinochlore with subordinate pennine (Supplementary Fig. 2). In backscattered electron images, the Fe-rich chlorites and Fe poor have the same texture (Fig. 3i). Rarely, apatite is interstitial with respect to chlorite and antigorite.

Native Cu with pure composition occurs as flames intergrown with antigorite (Figs. 6a and 6b; Table S7), along cleavage planes and along partially healed fractures cutting clinopyroxene (Fig. 6c). Occasionally, native copper occurs in fractures of chromian spinel as well as along chromian spinel grain boundaries (Fig. 6d). Occasionally, individual titanite grains are closely associated with native copper and chlorite (Fig. 6e) in zone III. Rare Cu-Au alloy is found in Zone III (Fig. 6e). Small inclusions of chalcocite (Cu_2S) are fully embedded within native copper (Fig. 6f). Chalcocites hosted by native copper as vein and inclusion shows a relatively narrow range of Cu (76.69-80.92 wt.%) and S (20.05-21.71 wt.%) (Table S7). Occasionally,

cadmium sulfides (Greenockite) occur as inclusions in native copper and have Cu (3.87-6.78 wt.%) and Cd contents (76.5-78.1 wt.%) (Table S7).

4.3. Chemical changes across the reaction zone

X-ray element mapping shows that the contact between Opx-rich and metasomatic zones (I and II) of Cu-rich pyroxenite samples is sharp (Fig. 7). The formation of amphiboles in Zone I is associated with increase in Ca, Na and Al. Sporadic high concentrations of these elements also occur in Zone II where they correspond to amphibole inclusions. Aluminium transfer may have also a significant role in the formation of chlorite in zone III. The high volumetric proportion of clinopyroxene in zone II is responsible for an increase in Ca.

4.4 Fluid inclusions in Zone II

A study of fluid inclusions (FIs) in clinopyroxene from zone II was carried out for the sample PX05 (Fig. 8a). FIs appear in cloudy clinopyroxenes either oriented randomly or along cleavage planes and healed cracks. The FIs mainly range in size from 3 to 10 μm and display various shapes (Fig. 8a). The inclusions are often partially or fully decrepitated and whiskers may occur (Fig. 8a). At room temperature two phases (liquid + vapor) can be observed (Fig. 8a). The FIs were discriminated based on their petrographic position following Roedder (1984) and Van den Kerkhof and Hein (2001). The FIs are considered to have a secondary origin, since they mostly occur along healed fractures and cleavage planes, indicating that they were captured after the formation of the host clinopyroxenes.

We determined the nature of the phases in the FIs using Raman microspectroscopy. The molar proportion of the fluid components (shown in Supplementary Table S8) in the fluid (vapor + liquid) at room temperature was calculated based on 1) the integrated band area of their

characteristic Raman bands and 2) Raman cross-sections following the method of Dubessy et al. (1989). In all studied FIs we identified CH_4 and H_2 based on their highest intensity bands (at ~2918; ~588 and ~4156 cm^{-1}, respectively) (Fig. 8b). The fraction of H_2 widely varies in the FIs from 20 to 98 vol.%.

4.5 U-Pb LA-ICP-MS dating of titanite

Laser ablation ICP-MS U-Pb analyses including U and Pb contents, isotopic ratios and ages of seven titanite grains from the Cheshmeh-Bid Cu-rich pyroxenite are given in Supplementary Table S9. All titanite grains contain some U ranging from 5 to 38 µg/g as well as some initial Pb. Concordia plots of titanite U–Pb isotopic results are shown in Figure 9. All titanite grains contain significant initial common Pb and therefore lie on a mixing line between the $^{207}Pb/^{206}Pb$ ratio of the common Pb component and the age of the radiogenic component as defined by the lower concordia intercept (Fig 9). Regressing data from the titanite grains using Isoplot (Ludwig, 2003) gives a line that projects to an age of 101±22 Ma. The MSWD of 3.8 indicates scatter outside of measurement error, probably because of excess variations in the Pb/U ratio. To some extent the 95% confidence error takes account of this since it scales as the square root of the MSWD (Ludwig, 2003).

4.6 Copper isotope composition of native copper

Copper isotopic results of eight native copper grains from the Cheshmeh-Bid Cu-rich pyroxenite are given in Supplementary Table S10. The eight native copper grains have Cu isotope compositions ranging from $\delta^{65}Cu$= -0.20 to +0.28‰ (Fig. 10). Errors for all the analyses are ± 0.08‰. An average $\delta^{65}Cu$ Bulk Silicate Earth (BSE) value of +0.07 ±0.10‰ (2SD) (Savage et al., 2015) was used to examine and characterize the Cu isotope composition of Cheshmeh-Bid native copper. The copper isotope values for the studied native copper lie

within the previously reported copper isotope range for bulk mantle rocks (Fig. 10; Ben Othman et al., 2006; Ikehata and Hirata, 2012; Liu et al., 2015; Zou et al., 2019). Native copper grains from the Cheshmeh-Bid pyroxenites display significant isotope fractionation compared to primary native copper in Horoman peridotite complex but there is significant isotope fractionation for Cheshmeh-Bid native copper.

4.7 Bulk-rock chemistry

Whole rock geochemical data of the Cheshmeh-Bid pyroxenite samples are shown in Supplementary Table S11. Compared to fresh pyroxenite samples (PX01 and PX20), matasomatized pyroxenites show slightly higher Mg# values (0.91-0.96), lower SiO_2 (46.37-51.76 wt.%), higher Al_2O_3 (2.60-8.84 wt.%), CaO (5.18-18.96 wt.%) and TiO_2 contents (0.07-0.17 wt.%) (Supplementary Table S11). The Cheshmeh-Bid metasomatised pyroxenites have high REE concentrations (3.79-15.64 µg/g).

We use in the following an isocon diagram of Grant (2005) to estimate element mobility associated with metasomatism in the Cheshmeh-Bid pyroxenites (Fig. 11). We used average composition of the Cheshmeh-Bid fresh orthopyroxenites (samples IRKJPX01 and IRKJPX20) and metasomatic pyroxenite samples (samples IRKJPX04, IRKJPX05, IRKJPX06, IRKJPX11 and IRKJPX12). The isocon diagrams allow to quantify the loss and gain of elements during the alteration of fresh samples by using TiO_2 and Sc to define the isocon (Fig. 11). These elements are commonly considered as relatively immobile during alteration (Van Baalen, 1993; Grant, 2005; Beinlich et al., 2010). The elements plotting above the isocon were gained during metasomatism, whereas those plotting below were lost. Concentration of Al_2O_3, CaO and REE increased during the metasomatism of the Cheshmeh-Bid orthopyroxenites, whereas MgO, FeO, SiO_2, MnO, K_2O and Ba decreased (Fig. 11). The slope of the constant composition line in the isocon diagram is 1.9. This indicates that the total mass and the total volume decreased

of 47 % and 61 % during the alteration, respectively. This is consistent with the observation that most major elements were lost during metasomatism.

4.8 Thermodynamic modelling of Ca-metasomatism

Thermodynamic modelling of phase equilibria indicates that the talc + antigorite + amphibole assemblage is stable in the presence of fluid at temperatures below ~ 420°C and at the lowest chemical potential of CaO investigated here (μCaO; Fig. 12). This assemblage is replaced at higher μCaO by amphibole + antigorite (I), then by clinopyroxene + antigorite (II) and finally by clinopyroxene + antigorite + chlorite (III). The samples having experienced Ca metasomatism are predicted to be composed of one of these three mineralogical assemblages (assemblage I for IRKJPX04 and assemblage III for IRKJPX11 and IRKJPX12). At the highest μCaO investigated in the simulation, phases such as brucite, wollastonite and vesuvianite are stable. These latter phases are not observed in the natural samples. The olivine-antigorite transition occurs at a higher temperature at low μCaO (450°C at -730 kJ/mol) than at high μCaO (250°C at -675 kJ/mol).

4.9 Stability of native copper

The Cu-Fe-Ni-O-S phase relations are displayed in Figure 13 as a function of the activities in $H_{2,aq}$ and $H_2S_{,aq}$ at 50 MPa and 200 °C, 300 °C and 400 °C. In the Fe-Ni-O-S system, the stability fields are identical to the ones calculated in Klein and Bach (2009). Native copper is stable at $a_{H2,aq} > 10^{-3}$ and $a_{H2S,aq} < 10^{-3}$ together with awaruite or heazlewoodite in the Cu-Fe-Ni-O-S system. Its stability field is bound by chalcocite (Cu_2S) at low $a_{H2S,aq}$ and bornite (Cu_5FeS_4) at higher $a_{H2S,aq}$. The stability field of bornite is bound by chalcopyrite ($CuFeS_2$) at $a_{H2S,aq} > 10^{-3}$ at 200°C and at $a_{H2S,aq} > 10^{-2}$ at 400°C. In the Cu-O-S system, the stability field of native copper extends towards higher $a_{H2S,aq}$ and is entirely bound by chalcocite.

5. Discussion

5. 1. Ca-metasomatism: the main driver for reaction zone formation

Thermodynamic calculations predict the progressive replacement of orthopyroxene by amphibole, clinopyroxene and chlorite as μCaO increases (Figure 12). This mineralogical sequence is exactly the one observed in the reaction zone where amphibole, clinopyroxene and clinopyroxene + chlorite are the main components of zones I, II and III, respectively (Fig. 3a). This suggests that calcium input is the main driver for metasomatism. Clinopyroxene crystals in zone II show a wide range of Mg# (0.76-0.98) due to almost unity Mg-Fe partition coefficient between clinopyroxene and associated antigorite and chlorites. Clinopyroxenes cogenetic with chlorites, antigorite and/or tremolite have metasomatic origin. Aluminum transfer may also play a role for the formation of zone III in which significant amounts of chlorite are observed. The chromian spinel of the orthopyroxenite appears to react during metasomatism and may provide the Al needed to form chlorite. Chromian spinel alteration may also explain the high Cr content measured in chlorite (up to 3.41 wt.%). The presence of chlorite inclusions and ferrian chromite in porous textured chromian spinel can be attributed to metamorphism or hydrothermal events (e.g. Beinlich et al 2020). Gervilla et al. (2012) suggested that during the early stage of chromite alteration, pristine chromite may react with olivine in the presence of reducing fluids to form chlorite and secondary high Cr-chromite with porous texture. Textural evidence (Fig. 3d) suggests the possibility that chromite grains from the Cheshmeh-Bid pyroxenites also reacted with percolating Ca^{2+}-H_2-rich fluids during metasomatism. Possible support for this scenario arises from the abundant large inclusions of chlorite and metasomatic clinopyroxene in porous chromian spinel rims.

Ca-metasomatism is thought to occur by interaction between the pristine orthopyroxenite and Ca-OH fluids derived from serpentinization of ultramafic rocks. The observation of

450 secondary/metamorphic olivine may also strengthen the interpretation of reaction zone
451 formation by Ca-metasomatism. The mode of occurrence and mineral chemistry of olivine
452 (Mg# = 0.75-0.83) in Opx-rich zone of Cu-rich pyroxenites is indeed in agreement with a
453 secondary origin. It is interesting to note that the Mg# of olivine is also controlled by the phases
454 in equilibrium (i.e. antigorite) and low-Mg# olivine is quite ordinary in low-T metaperidotites
455 (Arai and Oyama, 1981).
456 Several hypotheses have been proposed to explain the dehydration of serpentine producing
457 olivine: (i) injection of magma into meta-peridotites or -serpentinites (e.g. Vance and Dungan,
458 1977); (ii) Barrovian-type metamorphism (e.g. Evans, 1977). (iii) de-serpentinization in deep
459 portion of subducting slab that has been linked to intermediate-depth intraslab earthquake (e.g.
460 Hacker et al., 2003;; Plümper et al., 2017); (iv) in-situ dehydration of serpentinized mantle
461 within oceanic lithosphere prior to subduction and/or obduction processes (Iyer et al., 2010).
462 Figure 12 shows that serpentine breakdown occurs at temperatures above 400°C at 50 MPa at
463 low μCaO (-730 kJ/mol). This is in agreement with experimental constraints in the Mg-Si-O-
464 H system (Ulmer and Trommsdorff, 1999; Padrón-Navarta et al., 2010). Furthermore, the
465 addition of CaO significantly shifts the antigorite-olivine equilibrium towards lower
466 temperature (250°C at μCaO = -675 kJ/mol; Figure 12). The evolution of the modes of the
467 rock-forming minerals (Supplementary Fig. 2) indicates that the reaction of olivine formation
468 at high μCaO can be written in the Mg-Si-Ca-O-H system as:

469 $$3\ Mg_{48}Si_{34}O_{85}(OH)_{62} + 20\ CaO = 20\ CaMgSi_2O_6 + 62\ Mg_2SiO_4 + 93\ H_2$$

470 There is no evidence for high-pressure metamorphism in the studied pyroxenites. This suggests
471 that serpentine breakdown and olivine formation are the result of Ca-metasomatism rather than
472 heating at high-pressure in the Cheshmeh-Bid pyroxenites.

Fluids originated during serpentinization, usually referred as "serpentinization-buffered fluids", are Si-undersaturated and Ca-rich (e.g. Bach and Klein, 2009). The source of Ca is still a matter of debate and two ultimate sources have been suggested: (i) breakdown of pyroxenes during serpentinization, which may release Ca^{2+} into aqueous fluids (e.g. Coleman, 1967; Allen and Seyfried, 2003). Bach and Klein (2009) proposed that addition of Ca^{2+} from serpentinizing peridotite is likely driven by diffusive mass transfer in the form of hydroxo species ($CaOH^{+}$); (ii) external hydrothermal solutions (e.g. Hatzipanagiotou and Tsikouras, 2001). The isocon diagram (Fig. 11) confirms mobility of major elements and REE (La-Lu) during metasomatism. Significant increase of CaO and decrease of SiO_2 reflect the Ca-metasomatism reaction during alteration of the Cheshmeh-Bid orthopyroxenites. Although REEs are generally regarded as immobile elements during fluid-rock reaction, they can be mobilized during metasomatic process and hydrothermal alteration (e.g., Salvioli-Mariani et al., 2020). Composition of fluid(s), pH conditions of the fluid phase, availability of ligands in the aqueous fluids and water/rock ratio are key factors controlling the pronounced REE mobilization during hydrothermal alteration and/or metasomatic processes. The formation of calcite and apatite during Ca-metasomatism of the Cheshmeh-Bid pyroxenites is likely related to high activities in CO_3^{2-} and PO_4^{3-}, respectively. Complexation of LREE may be triggered by carbonate ions (e.g. Gimeno-Serrano et al., 2000). High concentration of LREE with respect to the HREE can be explained by preferential complexation of carbonates with LREE. High pH and relatively basic conditions are favourable for the REE-carbonate complexation (e.g. Haas et al., 1995), which is consistent with alkaline nature of fluids during serpentinization of peridotites (e.g. Barnes and O'Neil, 1969).

The Ca-metasomatism observed in the case of Cheshmeh-Bid Cu-rich pyroxenites leads to the formation of a reaction zone. The dykes are surrounded by harzburgites and dunites having experienced extensive serpentinization, suggesting that clinopyroxene breakdown in the

ultramafic rocks during hydration may play a key role for the Ca-metasomatism described here. In the following, we further investigate the links between Ca-metasomatism and serpentinization by looking at evidence for reducing conditions during fluid/rock interaction.

5. 2. Reducing conditions during metasomatism

Serpentinization leads to reducing conditions due to the coupled reduction of water to form H_2 and the oxidation of the ferrous iron initially contained in the primary minerals (mostly olivine) to form ferric minerals (e.g. magnetite) (McCollom and Bach, 2009; Malvoisin et al., 2012). H_2 (e.g. Barnes et al., 1967) is commonly observed in fluids associated with serpentinized peridotites and Ni-Fe alloys (e.g. Ramdohr, 1950) have been described in serpentinized peridotites. Methane is also found in serpentinizing environments; it is generated through reduction of CO_2 or CO by H_2 (e.g. Charlou et al., 2002; McCollom, 2016). The observation of H_2-CH_4-bearing fluid inclusions in metasomatic diopside from the Cheshmeh-Bid pyroxenites indicates that Ca-metasomatism occurred under reducing conditions, most likely associated with the serpentinization of the surrounding rocks.

The source of copper may be either desulfurization of primary Cu-sulpfides of the pyroxenite during the hydrothermal overprint or transportation of Cu in a S-poor fluid from the surrounding harzburgites-dunites into the orthopyroxenite dike during hydrothermal alteration. Thermodynamic modelling indicates that native copper can be stable at high H_2 activity and/or at a low H_2S activity (Fig. 13). The fluid inclusions data reveal the presence of H_2 during metasomatism (Figs. 8a and 8b), suggesting that a high activity in H_2 prevailed during native copper formation in the Cheshmeh-Bid pyroxenites. H_2S activity during alteration is probably relatively low (Fig. 13) and thus difficult to constrain. Some mineral equilibria allow H_2S activity to be retrieved from H_2 activity. Seyfried et al. (2004) proposed that a_{H2} and a_{H2S} may be buffered by the equilibrium magnetite + bornite + chalcocite in serpentinized peridotites.

Klein and Bach (2009) used mineralogical observations in serpentinized peridotites collected on the seafloor and measurements of H_2S and H_2 concentrations in fluids venting at peridotite-hosted hydrothermal fields (Rainbow and Logatchev, Charlou et al., 2002) to determine that the heazlewoodite/pentlandite equilibrium buffers a_{H2S} where serpentinization occurs (HP buffer). The sulfide mineralogy in the serpentinized peridotites surrounding the orthopyroxenites described here is dominated by pentlandite and heazlewoodite suggesting that the HP buffer may fix a_{H2} and a_{H2S} during native Cu formation. This would imply fast H_2 and H_2S transport between the serpentinized peridotites and the orthopyroxenites. H_2 is known to diffuse rapidly in water (Kallikragas et al., 2014). Figure 13 shows that native copper is not stable at a_{H2} and a_{H2S} fixed by the HP buffer in the Cu-Fe-Ni-O-S system. Bornite (Cu_5FeS_4) is indeed the stable Cu-bearing mineral along the HP buffer under reducing conditions. Bornite and other iron-bearing sulfides have not been observed in the samples from the Cheshmeh-Bid Ophiolite. This may be interpreted as evidence for i) a_{H2S} below the one fixed by the HP buffer or ii) a low iron availability preventing Fe-bearing sulfide formation in zone III during metasomatism (Fig. 13). It is difficult to select one of these two options since the mobility of H_2S and the availability of iron are poorly constrained in the studied system. The isocon diagram (Fig. 11) indicates that Fe is lost during metasomatism but the concentration in Fe is still sufficient to form bornite instead of native copper in zone III. The thermodynamic calculations performed here in the Cu-Fe-Ni-O-S system assume the presence of Fe in excess and thus do not allow for Fe distribution to be investigated. Thermodynamic calculation of iron distribution in a Cu-bearing system is theoretically possible, for example, with Gibbs energy minimization. However, it cannot be currently performed due to the lack of a thermodynamic database containing Cu-sulfides and realistic silicate solid solutions.

The scarcity of chalcocite in the studied samples and its occurrence as inclusions in native copper (Fig. 6f) suggest that native copper is formed at the expense of chalcocite during

alteration. If a_{H2S} is below the HP buffer (i), native copper formation can be explained by desulfurization induced by an increase in H_2 activity associated with serpentinization in the surrounding peridotites. If a low iron availability is assumed and bornite formation is excluded from thermodynamic calculations (ii), native Cu can be stable at the activities in $H_{2,aq}$ and $H_2S_{,aq}$ fixed by the HP buffer (Fig. 13), allowing the following equation to be written:

$$2\ Fe_{4.5}Ni_{4.5}S_8 + 12\ H_2O + 20\ Cu = 3\ Ni_3S_2 + 3\ Fe_3O_4 + 10\ Cu_2S + 12\ H_{2,aq}$$

2 Pentlandite + 12 H_2O + 20 Native Copper = 3 Heazlewoodite + 3 Magnetite + 10 Chalcocite + 12 $H_{2,aq}$

This equilibrium can be used to estimate the minimum aH_2 achieved during native copper formation (see Fig. 13-14). Klein and Bach (2009) estimated that H_2 gas could be produced after saturation in the liquid during serpentinization providing an estimate for a_{H2} variation with temperature (Fig. 14). If a_{H2} is fixed on the gas saturation line, native Cu is stable at temperature below ~ 325 °C, whereas chalcocite is stable at higher temperature. Native Cu may thus be formed through chalcocite desulfurization associated with a decrease in temperature.

5.3. Model of native copper formation: Ca-metasomatism at the seafloor in a supra-subduction setting

5.3.1. Cu isotope constraints on the Cu provenance

The copper isotope values for the studied native copper are similar to those reported for bulk mantle rocks (Fig. 10; Ben Othman et al., 2006; Ikehata and Hirata, 2012; Liu et al., 2015; Zou et al., 2019). As discussed above, native Cu formation in the Cheshmeh-Bid pyroxenites can be related to addition of external Cu or desulfurization of pre-existing Cu sulfides. These two hypotheses can be assessed by copper isotopes of other mafic-ultramafic lithologies. Copper sourced from the surrounding mafic ophiolitic rocks provides the most straightforward interpretation of the data. The study by Dekov et al. (2013) augments this interpretation. In their study of native

572 copper associated with modern oceanic crust, they proposed that Cu was mobilized within the
573 basalts with no significant copper fractionation, whereas highly fractionated copper derived
574 from seawater was found in the sedimentary sections of the drilled cores. Ikehata and Hirata
575 (2012) also showed copper isotope value of primary native copper in peridotite was same as
576 that of the host rock and demonstrated that there was no significant copper isotope fractionation
577 during high-temperature magmatic processes.
578 In-situ alteration of the copper sulfides by metamorphic fluid certainly occurred and could have
579 impacted the copper isotope values in the native copper. How metamorphic fluids could alter
580 the copper isotope composition in this tectonic environment are not well studied, however,
581 Höhn et al. (2017) demonstrated that the metamorphic processes associated with sulfide
582 deposition generated a relatively tight range of copper isotope value from -0.3 to +0.4 ‰.
583 Equally interesting and related to the formation of native copper in association with basalts,
584 the Michigan native copper associated with secondary mobilization of copper also display a
585 relatively tight range of copper isotope values that overlap the values reported here (Bornhorst
586 and Mathur, 2017; Larson et al., 2003; Mathur et al., 2014). Therefore, significant copper
587 isotope fractionation could not have occurred during secondary alteration by metamorphic
588 fluids. This interpretation is in agreement with the textural and thermodynamic evidence
589 discussed.
590 Most certainly, the copper isotope values seen in the native copper samples are not related to
591 secondary supergene processes or high temperature magmatic processes. Baggio et al. (2017)
592 demonstrated that copper sourced from local basalts was later redistributed through supergene
593 process that causes the 2 ‰ variation measured. Mathur et al. (2005) and Mathur et al. (2009a)
594 clearly show that highly fractionated copper isotope values in supergene minerals resulted from
595 low temperature oxidation. Ikehata et al. (2011) found that copper isotope values of supergene

native copper (from +1.4 to +1.7 ‰) were significantly higher than those of primary chalcopyrite (from -0.3 to -0.1 ‰) from the same deposit.

Due to textural equilibrium of the Cheshmeh-Bid native copper with antigorite and chlorite, high temperature magmatic processes suggested by Ikehata and Hirata (2012) for the primary native copper in the peridotite are unlikely for its formation. Zou et al. (2019) suggested that remarkable copper isotope heterogeneity for Balmuccia pyroxenites is due to variable extent of sulfide segregation as well as melt-peridotite reaction. The absence of any main sulfide phases (e.g. pentlandite, chalcopyrite and pyrrhotite) in the Cheshmeh-Bid pyroxenites precludes the possibility of magmatic sulfide segregation and/or melt-peridotite reaction. Unfortunately, we could not obtain the copper isotope values of the magmatic chalcocite grains because they are very small (Fig. 6f). However, the chalcocites probably has the same δ^{65}Cu values to bulk mantle rocks. Previous studies of copper isotope values of sulfide minerals from igneous-hosted ore deposits are tightly clustered around 0 ‰ (–0.6 to 0.4 ‰) (e.g. Larson et al., 2003).

Our petrographic and geochemical results show that metasomatic fluids were involved for the formation of the Cheshmeh-Bid native copper. Copper isotope variations of native copper grains from the Cheshmeh-Bid pyroxenites are slightly large in comparison with those of non-metasomatised peridotite (Fig. 10; Ben Othman et al., 2006; Ikehata and Hirata, 2012; Liu et al., 2015), probably due to Cu isotope heterogeneity of the magmatic chalcocite grains and isotope fractionations during desulfurization of the sulfides. Our study also indicates that Cu isotopes can be a powerful tool to trace the source of copper in ophiolitic rocks.

5.3. 2. Timing of copper formation

Based on $^{40}Ar/^{39}Ar$ dating on hornblendes from plagiogranites and diabase, the genesis of Neyriz ophiolite in the southeast of Neyriz/Khajeh-Jamali ophiolite belt was constrained to

621 Late Cretaceous (range between 83.6 ± 8.4 Ma and 93.19 ± 2.48 Ma) (Lanphere and Pamić,
622 1983; Babaie et al., 2006). U-Pb zircon dating of plagiogranite and gabbro intrusions provided
623 formation ages of 100.1 ± 2.3 to 93.4 ± 1.3 Ma for the Neyriz ophiolite (Monsef et al., 2018).
624 The nature and formation age of Khajeh-Jamali ophiolitic massifs in the northwest of
625 Neyriz/Khajeh-Jamali ophiolite belt remains currently debated. The uncertainty of
626 geochronological data for the Khajeh-Jamali ophiolitic massifs made it difficult to understand
627 the formation age of these massifs. Uranium–lead dating carried out in this study on titanite
628 grains in association with native copper yield an age of 101±22 Ma (Fig. 9) which may be thus
629 considered as the age of copper mineralization. If the previously reported age interval
630 (83.6 ± 8.4 Ma-100.1 ± 2.3 Ma) could be attributed to the Khajeh-Jamali ophiolitic massifs,
631 our U-Pb geochronological data on titanite indicates seafloor serpentinization, Ca-
632 metasomatism and native copper precipitation during formation of an intra-oceanic forearc
633 setting.
634
635 5.3.3 A model for copper formation
636 Considering all available data, a genetic model is proposed for the formation of native Cu
637 occurrence during Ca-metasomatism affecting orthopyroxenites (Fig. 15). High Cr-spinels of
638 the studied pyroxenites bear remarkable chemical resemblance to the peridotites and mantle-
639 hosted chromitites from the studied area (Fig. 5). High Cr#, low TiO_2 content of the Cheshmeh-
640 Bid pyroxenites are consistent with crystallization from arc-related magmas such as high-Mg
641 andesite or boninite. At the first stage, orthopyroxenite dykes formed by magmatic segregation
642 from Mg-andesite or boninite melts within a supra-subduction mantle at oceanic-arc system.
643 At the second stage, the associated mantle peridotites underwent sub-sea floor hydrothermal
644 alteration. Mantle exhumation was possibly enhanced by the trench-slab roll-back system (e.g.
645 Barth et al., 2008). In such a scenario, Ca^{2+} and H_2 released from the serpentinizing peridotite

metasomatised ultramaficafic lithologies (here pyroxenite dykes). Circulation of hydrothermal fluids formed reaction zones I (amphibole + antigorite), II (clinopyroxene + antigorite) and III (clinopyroxene + chlorite + antigorite), respectively. During late stage of sea-floor serpentinization, native copper was likely formed by low-temperature alteration of Cu-sulfides in the pyroxenites at highly reducing conditions.

6. Concluding remarks

Alteration of pyroxenites from the Cheshmeh-Bid massif led to the formation of a reaction zone composed of three distinct metasomatic mineral assemblages (i) amphibole + antigorite (ii) clinopyroxene + antigorite and (iii) clinopyroxene + chlorite + antigorite (III). Metasomatism was driven by calcium transport and low $aSiO_2$ fluids which could be related to interaction with Ca-rich fluids formed during clinopyroxene breakdown in the surrounding serpentinized peridotites. The fluid inclusions data reveal the presence of H_2 inclusions along the cleavage planes and healed cracks of clinopyroxenes in Zone II, revealing that a high activity in H_2 prevailed during native copper formation in the Cheshmeh-Bid pyroxenites. These observations are consistent with thermodynamic calculations showing that native copper can be stable at high H_2 activity. The reducing conditions associated with serpentinization allowed for native copper formation under decreasing T conditions. Tightly clustered copper isotope values of native copper also indicate secondary alteration by metamorphic fluids. According to the Cu isotope composition, a mantle origin can be inferred for copper. Serpentinization and Ca-metasomatism likely occurred in an intra-oceanic forearc setting during Albian.

Acknowledgments

We would like to thank the two anonymous reviewers, and the editor Marco Scambelluri for their constructive and valuable comments and suggestions on our manuscript. Valentina

671 Batanova and Valérie Magnin (ISTerre) are thanked for their help during the electron
672 microprobe measurements. We would like to express our sincere gratitude to local people in
673 Khajeh-Jamali village and workers from the Fars Chromite Company. The work of L. E. Aradi
674 and Cs. Szabó was supported by the ELTE Institutional Excellence Program (TKP2020-IKA-
675 05) managed by the Hungarian Ministry of Human Capacities. The work of G. Grieco was
676 supported by the Italian Ministry of Education (MIUR) through the projects "PRIN2017 -
677 Mineral reactivity, a key to understand large-scale processes" (2017L83S77) and "Dipartimenti
678 di Eccellenza 2018-2022". C.M.´s research has been funded by project PID2019-111715GB-
679 I00 / AEI / 10.13039/501100011033.
680

681 **References**

682 Abrajano, T.A., Pasteris, J.D., 1989. Zambales ophiolite, Philippines. II. Sulfide petrology of
683 the critical zone of the Acoje Massif. Contributions to Mineralogy and Petrology 103, 64–77.
684
685 Abrajano, T.A., Sturchio, N.C., Bohlke, J.K., Lyon, G.L., Poreda, R.J., Stevens, C.M., 1988.
686 Methane-hydrogen gas seeps, Zambales Ophiolite, Philippines: Deep or shallow origin?
687 Chemical Geology 71, 211-222.
688
689 Alavi, M., 1994. Tectonics of the Zagros orogenic belt of Iran: new data and interpretations.
690 Tectonophysics 229, 211–238.
691
692 Allen, D.E., Seyfried Jr, W.E., 2003. Compositional controls on vent fluids from ultramafic-
693 hosted hydrothermal systems at mid-ocean ridges: An experimental study at 400°C, 500 bars.
694 Geochimica et Cosmochimica Acta 67, 1531-1542.
695

Arai, S., Oyama, T., 1981. Unusual olivine in peridotite from Ochiai-Hokubo ultramafic complex, western Japan. Annual Report of the Institute of Geoscience, the University of Tsukuba 7, 70-73.

Babaie, H.A., Babaei, A., Ghazi, A.M., Arvin, M., 2006. Geochemical,$^{40}Ar/^{39}Ar$ age, and isotopic data for crustal rocks of the Neyriz ophiolite, Iran. Canadian Journal of Earth Sciences 43, 57–70.

Bach, W., Klein, F., 2009. The petrology of seafloor rodingites: insights from geochemical reaction path modeling. Lithos 112, 103–117.

Baggio, S. B., Hartmann, L. A., Lazarov, M., Massonne, H.-J., Opitz, J., Theye, T., Viefhaus, T., 2017. Origin of native copper in the Paraná volcanic province, Brazil, integrating Cu stable isotopes in a multi-analytical approach. Mineralium Deposita 53, 417–434.

Barnes, I., Lamarche, V.C., Himmelberg, G., 1967. Geochemical evidence of present-day serpentinization. Science 156, 830–832.

Barnes, I., O'Neil, J.R., 1969. The relationship between fluids in the fresh alpine-type ultramafics and possible modern serpentinization, western United States. Bulletin of the Geological Society of America 80, 1947–1960.

Ben Othman, D., Luck, J.M., Bodinier, J.L., Arndt, N.T., Albarède, F., 2006. Cu–Zn isotopic variations in the Earth's mantle. Geochimica et Cosmochimica Acta 70, A46.

721 Barth, M.G., Mason, P.R.D., Davies, G.R., Drury, M.R., 2008. The Othris Ophiolite, Greece:
722 a snapshot of subduction initiation at a mid-ocean ridge. Lithos 100, 234–254.
723
724 Beinlich, A., Klemd, R., John, T., Gao, J., 2010. Trace-element mobilization during Ca-
725 metasomatism along a major fluid conduit: Eclogitization of blueschist as a consequence of
726 fluid–rock interaction. Geochimica et Cosmochimica Acta 74(6), 1892-1922.
727
728 Beinlich, A., Heydebrand, A., Klemd, R., Martin, L., Hicks, J., 2020. Desulphurisation,
729 chromite alteration, and bulk rock PGE redistribution in massive chromitite due to
730 hydrothermal overprint of the Panton Intrusion, east Kimberley, Western Australia. Ore
731 Geology Reviews 118, 103-288.
732
733 Bornhorst, T., Mathur, R., 2017. Copper isotope constraints on the genesis of the Keweenaw
734 Peninsula native copper district, Michigan, USA. Minerals 7(10), 185.
735
736 Cabral, A.R., Beaudoin, G., 2007. Volcanic red-bed copper mineralisation related tosubmarine
737 basalt alteration, Mont Alexandre, Quebec Appalachians, Canada. Mineralium Deposita 42,
738 901–912.
739
740 Charlou, J.L., Donval, J.P., Fouquet, Y., Jean-Baptiste, P., Holm, N., 2002. Geochemistry of
741 high H_2 and CH_4 vent fluids issuing from ultramafic rocks at the Rainbow hydrothermal field
742 (36 14′ N, MAR). Chemical geology 191(4), 345-359.
743

744 Connolly, J.A., 2005. Computation of phase equilibria by linear programming: a tool for
745 geodynamic modeling and its application to subduction zone decarbonation. Earth and
746 Planetary Science Letters 236(1-2), 524-541.
747
748 Coleman, R.G., 1967. Low-temperature reaction zones and alpine ultramafic rocks of
749 California, Oregon, and Washington. U.S. Geological Survey Bulletin 1247, 1–49.
750
751
752 Davis, D. W., Edwards, G. R., 1986. Crustal evolution of Archean rocks in the Kakagi Lake
753 area, Wabigoon Subprovince, Ontario, as interpreted from high-precision U–Pb
754 geochronology. Canadian Journal of Earth Sciences 23(2), 182-192.
755 https://doi.org/10.1139/e86-021
756
757 Dekov, V.M., Rouxel, O., Asael, D., Hålenius, U., Munnik, F., 2013. Native Cu from the
758 oceanic crust: Isotopic insights into native metal origin. Chemical Geology 359, 136-149.
759
760 Diener, J.F.A., Powell, R., White, R.W., Holland, T.J.B., 2007. A new thermodynamic model
761 for clino- and orthoamphiboles in the system Na_2O-CaO-FeO-MgO-Al_2O_3-SiO_2-H_2O-O.
762 Journal of Metamorphic Geology 25, 631-56.
763
764 Dubessy, J., Poty, B., Ramboz, C., 1989. Advances in COHNS fluid geochemistry based on
765 micro-Raman spectrometric analysis of fluid inclusions. European journal of Mineralogy 1(4),
766 517-534.
767

768 Eslami, A., Ghaderi, M., Griffin, W.L., Gain, S., Grieco, G., González-Jiménez, J.M., 2015.
769 Magmatic and post-magmatic signatures of chromian spinels in podiform chromitites from the
770 Cheshmeh-Bid chromitite deposit, Khajeh-Jamali Ophiolitic Massifs. Iran. Ofioliti 40 (2), 91–
771 106.
772
773 Eslami, A., 2015. Mineralogy, geochemistry and genesis of chromite and platinum group
774 minerals at Cheshmeh-Bid chromite deposit, Neyriz ophiolite. MSc thesis, Tarbiat Modares
775 University.
776
777 Evans, B.W., 1977. Metamorphism of alpine peridotite and serpentinite. Annual Review of
778 Earth and Planetary Sciences 5, 397-447.
779
780 Gervilla, F., Padrón-Navarta, J., Kerestedjian, T., Sergeeva, I., González-Jiménez, J., Fanlo, I.,
781 2012. Formation of ferrian chromite in podiform chromitites from the Golyamo Kamenyane
782 serpentinite, Eastern Rhodopes, SE Bulgaria: a two-stage process. Contributions to Mineralogy
783 and Petrology 164, 1–15.
784
785 Gimeno-Serrano, M.J., Sanz, L.F.A., Nordstrom, D.K., 2000. REE speciation in low
786 temperature acidic waters and the competitive effects of aluminium. Chemical Geology 165,
787 167–180.
788
789 Grant, J.A., 2005. Isocon analysis: a brief review of the method and applications. Physics and
790 Chemistry of the Earth 30, 997–1004.
791

792 Govindaraju, K., 1994. Compilation of working values and sample description for 383
793 geostandards. Geostandards Newsletter 18, 1–158.
794
795 Gunia, P., 1986. Native copper from rodingitized gabbroic dykes in serpentinites of the
796 Braszowice-BrzeŸnica massif (Lower Silesia). Mineralogia Polonica 17, 63–76.
797
798 Haas, J.R., Shock, E.L., Sassani, D.C., 1995. Rare earth elements in hydrothermal systems:
799 estimates of standard partial melting modal thermodynamic properties of aqueous complexes
800 of the rare earth elements at high pressures and temperatures. Geochimica et Cosmochimica
801 Acta 59, 4329–4350.
802
803 Hatzipanagiotou, K., Tsikouras, B., 2001. Rodingite formation from diorite in the Samothraki
804 ophiolite, NE Aegean, Greece. Geological Journal 36, 93–109.
805
806 Hacker, B.R., Peacock, S.M., Abers, G.A., Holloway, S.D., 2003. Subduction factory-2. Are
807 intermediate-depth earthquakes in subducting slabs linked to metamorphic dehydration
808 reactions? Journal of Geophysical Research-Solid Earth 108, doi:10.1029/2001JB001129.
809
810 Holland, T., Powell, R., 1996. Thermodynamics of order-disorder in minerals. 2. Symmetric
811 formalism applied to solid solutions. American Mineralogist 81, 1425-37.
812
813 Holland, T.J.B., Powell, R., 1998a. An internally consistent thermodynamic data set for phases
814 of petrological interest. Journal of Metamorphic Geology 16, 309-43.
815

816 Holland, T., Baker, J., Powell, R., 1998b. Mixing properties and activity-composition
817 relationships of chlorites in the system MgO-FeO-Al_2O_3-SiO_2-H_2O. European Journal of
818 Mineralogy 10, 395-406.
819
820 Höhn, S., Frimmel, H. E., Debaille, V., Pašava, J., Kuulmann, L., and Debouge, W., 2017. The
821 case for metamorphic base metal mineralization: pyrite chemical, Cu and S isotope data from
822 the Cu-Zn deposit at Kupferberg in Bavaria, Germany. Mineralium Deposita 52, 1145–1156.
823
824 Ikehata, K., Notsu, K., Hirata, T., 2011. Copper isotope characteristics of copper-rich minerals
825 from Besshi-type volcanogenic massive sulfide deposits, Japan, determined using a
826 femtosecond LA-MC-ICP-MS. Economic Geology 106, 307–316.
827
828 Ikehata, K., Hirata, T., 2012. Copper isotope characteristics of copper-rich minerals from the
829 Horoman peridotite complex, Hokkaido, northern Japan. Economic Geology 107, 1489–1497.
830
831 Ikehata, K., Chida, K, Tsunogae, T., Bornhorst, T.J., 2016, Hydrothermal native copper in
832 Ocean Island Alkali basalt from the Mineoka Belt, Boso Peninsula, Central Japan. Economic
833 Geology 111, 783–794.
834
835 Ionov, D.A., Savoyant, L., Dupuy, C., 1992. Application of the ICP-MS technique to trace
836 element analysis of peridotites and their minerals. Geostandards Newsletter 16(2), 311-315.
837
838 Iyer, K., Rupke, L.H., Morgan, J.P., 2010. Feedbacks between mantle hydration and
839 hydrothermal convection at ocean spreading centers. Earth and Planetary Science Letters 296,
840 34-44.

Jochum, K.P., Weis, U., Schwager, B., Stoll, B., Wilson, S.A., Haug, G.H., Andreae, M.O., Enzweile, J., 2016. Reference values following ISO guidelines for frequently requested rock reference materials. Geostandards and Geoanalytical Research 40(3), 333-350.

Johnson, J.W., Oelkers, E.H., Helgeson, H.C., 1992. SUPCRT92: A software package for calculating the standard molal thermodynamic properties of minerals, gases, aqueous species, and reactions from 1 to 5000 bar and 0 to 1000 C. Computers and Geosciences 18(7), 899-947.

Kallikragas, D. T., Plugatyr, A. Y., Svishchev, I. M., 2014. High temperature diffusion coefficients for O_2, H_2, and OH in water, and for pure water. Journal of Chemical and Engineering Data 59(6), 1964-1969.

Klein, F., Bach, W., 2009. Fe–Ni–Co–O–S phase relations in peridotite–seawater interactions. Journal of Petrology 50(1), 37-59.

Lanphere, M.A., Pamić, J., 1983. $^{40}Ar^{39}Ar$ ages and tectonic setting of ophiolite from the Neyriz area, southeast Zagros Range, Iran. Tectonophysics 96, 245–256.

Larson, P. B., Maher, K., Ramos, F. C., Chang, Z., Gaspar, M., Meinert, L. D., 2003. Copper isotope ratios in magmatic and hydrothermal ore-forming environments. Chemical Geology 201, 337-350.

Leake, B., Woolley, A., Arps, C., Birch, W., Gilbert, M.C., Grice, J.D., Hawthorne, F.C., Kato, A., Kisch, H.J., Krivovichev, V.G., Linthout, K., Laird, J., Mandarino, J.A., Maresch, W.V.,

866 Nickel, E.H., Rock, N.M.S., Schumacher, J.C., Smith, D.C., Ungaretti, L., Whittaker, E.J.W.,
867 Youzhi, G., 1997. Nomenclature of Amphiboles; Report of the Subcommittee on Amphiboles
868 of the International Mineralogical Association Commission on New Minerals and Mineral
869 Names. Mineralogical Magazine 61(405), 295-310. doi:10.1180/minmag.1997.061.405.13.
870
871 Liu, S.-A., Huang, J., Liu, J., Wörner, G., Yang, W., Tang, Y., Chen, Y., Tang, L., Zheng, J.,
872 Li, S., 2015. Copper isotopic composition of the silicate Earth. Earth and Planetary Science
873 Letters 427, 95-103.
874
875 Lorand, J.P., Gregoire, M., 2006. Petrogenesis of base metal sulphide assemblages of some
876 peridotites from the Kaapvaal craton (South Africa). Contribution to Mineralogy and Petrology
877 151(5), 521–538.
878
879 Ludwig, K.R., 2003. User's manual for Isoplot 3.00: a geochronological toolkit for Microsoft
880 Excel. Berkeley Geochronology Center Special Publication No. 4, 71 pp.
881
882 Malvoisin, B., Carlut, J., Brunet, F., 2012. Serpentinization of oceanic peridotites: 1. A high-
883 sensitivity method to monitor magnetite production in hydrothermal experiments. Journal of
884 Geophysical Research-Solid Earth 117(B1).
885
886 Mathur, R., Ruiz, J., Titley, S., Liermann, L., Buss, H., Brantley, S. L., 2005. Cu isotopic
887 fractionation in the supergene environment with and without bacteria. Geochimica et
888 Cosmochimica Acta 69(22), 5233-5246.
889

Mathur, R., Titley, S., Barra, F., Brantley, S., Wilson, M., Phillips, A., Munizaga, F., Maksaev, V., Vervoort, J., Hart, G., 2009a. Exploration potential of Cu isotope fractionation in porphyry copper deposits. Journal of Geochemical Exploration 102, 1-6.

Mathur, R., Titley, S., Hart, G., Wilson, M., Davignon, M., Zlatos, C., 2009b. The history of the United States cent revealed through copper isotope fractionation. Journal of Archaeological Science 36(2), 430-433.

Mathur, R., Wilson, M., Parra, M. L., 2014. Challenges of using copper isotope ratios to trace the origin of native copper artifacts: An example from the Keweenaw Peninsula. Annals of Carnegie Museum 82, 241-245.

McCollom, T.M., Bach, W., 2009. Thermodynamic constraints on hydrogen generation during serpentinization of ultramafic rocks. Geochimica et Cosmochimica Acta 73, 856– 875, doi:10.1016/j.gca.2008.10.032.

McCollom, T.M., 2016. Abiotic methane formation during experimental serpentinization of olivine. Proceedings of the National Academy of Sciences 113, 13965-13970.

Monsef, I., Monsef, R., Mata, J., Zhang, Z., Pirouz, M., Rezaeian, M., Esmaeili, R., Xiao, W., 2018. Evidence for an early-MORB to fore-arc evolution within the Zagros suture zone: Constraints from zircon U-Pb geochronology and geochemistry of the Neyriz ophiolite (South Iran). Gondwana Research 62, 287-305.

914 Miura, M., Arai, S., 2014. Platinum-group element and mineral characteristics of sub-arc
915 chromitite xenoliths from the Takashima alkali basalt, southwest Japan Arc. Canadian
916 Mineralogist 52, 899–916.
917
918 Nagle, F., Fink, L.K., Boström, K., Stipp, J.J., 1973. Copper in pillow basalts from La Desirade,
919 Lesser Antilles island arc. Earth and Planetary Science Letters 19, 193–197.
920
921 Padrón-Navarta, J. A., Hermann, J., Garrido, C. J., Sánchez-Vizcaíno, V. L., Gómez-Pugnaire,
922 M. T., 2010. An experimental investigation of antigorite dehydration in natural silica-enriched
923 serpentinite. Contributions to Mineralogy and Petrology 159(1), 25.
924
925 Padrón-Navarta, J.A., López-Sánchez-Vizcaíno, V., Hermann, J., Connolly, J.A., Garrido,
926 C.J., Gómez-Pugnaire, M. T., Marchesi, C., 2013. Tschermak's substitution in antigorite and
927 consequences for phase relations and water liberation in high-grade
928 serpentinites. Lithos 178, 186– 196.
929
930 Plümper, O., John, T., Podladchikov, Y. Y., Vrijmoed, J. C., Scambelluri, M., 2017. Fluid
931 escape from subduction zones controlled by channel-forming reactive porosity. Nature
932 Geoscience 10(2), 150.
933
934 Ramdohr, P., 1950. Über Josephinite, Awaruite, Souesite, ihre Eigenschaften, Enstehungund
935 Paragensis. Mineralogical Magazine 29, 374–394.
936

937 Rajabzadeh, M.A., 1998. Mineralisation en chromite et elements du groupe du platinedans les
938 ophiolitesd'Assemion et de Neyriz, centrure du Zagros, Iran. Ph.D. Thesis, Institute National
939 Polytechnique de Lorraine, France, 358 pp.
940
941 Rajabzadeh, M.A., Nazari-Dehkordi, T., 2013. Investigation on mantle peridotites from Neyriz
942 ophiolite, south of Iran: geodynamic signals. Arabian Journal of Geosciences 6, 4445-4461.
943
944 Roedder, E., 1984. Fluid inclusions. Reviews in Mineralogy 12, Mineralogical Society of
945 America, 644 p.
946
947 Salvioli-Mariani, E., Boschetti, T., Toscani, L., Montanini, A., Petriglieri, J.R., Bersani, D.,
948 2020. Multi-stage rodingitization of ophiolitic bodies from Northern Apennines (Italy):
949 Constraints from petrography, geochemistry and thermodynamic modelling. Geoscience
950 Frontiers 11 (6), 2103-2125.
951
952 Savage, P.S., Moynier, F., Chen, H., Shofner, G., Siebert, J., Badro, J., Puchtel, I.S., 2015.
953 Copper isotope evidence for large-scale sulphide fractionation during Earth's differentiation.
954 Geochemical Perspectives Letters 1(0), 53-64.
955
956 Seyfried Jr, W.E., Foustoukos, D.I., Allen, D.E., 2004. Ultramafic-hosted hydrothermal
957 systems at mid-ocean ridges: chemical and physical controls on pH, redox and carbon reduction
958 reactions. In: German, C. R., Lin, J. and Parson, L. M. (eds.) Mid-Ocean Ridges: Hydrothermal
959 Interactions Between the Lithosphere and Oceans 148, American Geophysical Union:
960 Geophysical Monograph 267-284.
961

962 Schwarzenbach, E.M., Gazel, E., Caddick, M.J., 2014. Hydrothermal processes in partially
963 serpentinized peridotites from Costa Rica: evidence from native copper and complex sulfide
964 assemblages. Contributions to Mineralogy and Petrology 168, 1079.
965
966 Shafaii Moghadam, H., Stern, R.J., 2015. Ophiolites of Iran: Keys to understanding the tectonic
967 evolution of SW Asia: (II) Mesozoic ophiolites. Journal of Asian Earth Sciences 100, 31-59.
968
969 Ulmer, P;, Trommsdorff, V., 1999. Phase relations of hydrous mantle subducting to 300 km.
970 In: Fei Y, Bertka CM, Mysen BO (eds) Mantle petrology: field observations and high pressure
971 experimentation. Special Publication No. 6. The Geochemical Society, Houston, pp 259–281.
972
973 Van Acken, D., Becker, H., Walker, R.J., McDonough, W.F., Wombacher, F., Ash, R.D.,
974 Piccoli, P.M., 2010. Formation of pyroxenite layers in the Totalp ultramafic massif (Swiss
975 Alps) – Insights from highly siderophile elements and Os isotopes. Geochimica et
976 Cosmochimica Acta 74, 661–683.
977
978 Van Baalen, M.R., 1993. Titanium mobility in metamorphic systems: a review. Chemical
979 Geology 110(1-3), 233-249.
980
981 Van den Kerkhof, A.M., Hein, U.F., 2001. Fluid inclusion petrography. Lithos 55, 27–47
982
983 Vance, J.A., Dungan, M.A., 1977. Formation of peridotites by deserpentinization in the
984 Darrington and Sultan areas, Cascade Mountains, Washington. Geological Society of America
985 Bulletin 88, 1497-1508.
986

Wall, A. J., Mathur, R., Post, J. E., Heaney, P. J., 2011. Cu isotope fractionation during bornite dissolution: An in situ X-ray diffraction analysis. Ore Geology Reviews 42(1), 62-70.

White, R.W., Powell, R., Holland, T.J.B., Worley, B.A., 2000. The effect of TiO_2 and Fe_2O_3 on metapelitic assemblages at greenschist and amphibolite facies conditions: mineral equilibria calculations in the system K_2O-FeO-MgO-Al_2O_3-SiO_2-H_2O-TiO_2-Fe_2O_3. Journal of Metamorphic Geology 18, 497-511.

Zou, Z., Wang, Z., Li, M., Becker, H., Geng, X., Hu, Z., Lazarov, M., 2019. Copper isotope variations during magmatic migration in the mantle: insights from mantle pyroxenites in Balmuccia peridotite massif. Journal of Geophysical Research: Solid Earth 124 (11), 11130-11149.

Figure captions

Fig. 1. a. Map of Mesozoic ophiolites of Iran, showing the Khajeh-Jamali ophiolitic massifs (within red square) in the Zagros Suture Zone; b. simplified geological map of Khajeh-Jamali area (modified after Rajabzadeh, 1998).

Fig 2. Hand samples of: a-b: partly metasomatised pyroxenite with native copper mineralization; c: highly metasomatised and deformed pyroxenite containing native copper mineralization. Scale of clips is 2 cm in length. Opx-rich zone is composed of orthopyroxene and minor clinopyroxene.

Fig. 3. Back-scatter-electron (BSE) images of the Cheshmeh-Bid Cu-rich pyroxenites. (a) Whole profile from Opx-rich portion and metasomatic zones (I) amphibole (Amp) + antigorite (Atg), (II) clinopyroxene (Cpx)+ antigorite and (III) clinopyroxene + chlorite (Chl) + antigorite. Zone I (antigorite+amphibole) is characterized by small narrow selvage of amphibole and antigorite; (b) Ovoid and lamellae inclusions of clinopyroxene in orthopyroxene; (c) Spinifex-liked textured olivine (Ol) in the middle of antigorite; (d) Sieve-textured chromite (Chr) included in orthopyroxene (Opx); (e) Euhedral inclusions of chlorite and clinopyroxene in chromite; (f) Zoned clinopyroxene in Zone II; (g) Inclusions of amphibole and orthopyroxene in metasomatic clinopyroxene; (h) Pseudomorph of clinopyroxene replaced by antigorite, chlorite and calcite; (i) Replacement of orthopyroxene by calcite (Cal); (j) Fe-poor (dark grey) and Fe-rich (light grey) chlorite.

1034 Fig. 4. Chemical compositions of olivines from the Cheshmeh-Bid peridotites. a Mg# vs. MnO
1035 (wt.%); b. Mg# vs. NiO (wt.%). The olivine compositions from the Cheshmeh-Bid dunites and
1036 harzburgites (Rajabzadeh and Nazari-Dehkordi, 2013) are included for comparison.
1037
1038 Fig. 5. Composition of Cr-spinels from the Cheshmeh-Bid orthopyroxenites. (a) Compositional
1039 plot of Cr-spinels on the Cr-Al-Fe^{3+}.ternary diagram (b) Cr/(Cr+Al) vs. Mg/(Mg+Fe^{2+}) (c)
1040 Cr/(Cr+Al) vs. TiO_2 (wt.%). Compositional fields of Cr-spinel from abyssal peridotites, forearc
1041 peridotites and podiform chromitites (Miura and Arai, 2014) are shown for comparison.
1042
1043 Fig. 6. Photomicrograph and back-scatter-electron (BSE) images of copper assemblage (zone
1044 III): (a-b) Reflected light (a) and cross polarized (b) images of native copper (Cu) intergrown
1045 with antigorite (Atg); (c) Native Cu along cleavage planes and along partially healed fractures
1046 cutting clinopyroxene (Cpx); (d) native copper filling fracture of chromian spinel (Chr); (e)
1047 association of Cu, Cu-Au alloy and titanite (Ttn) in metasomatic clinopyroxene. Cu and Au
1048 maps are shown as small insets; (f) chalcocite (Cct) inclusions in native copper.
1049
1050 Fig. 7. Back-scattered electron (BSE) imaging and multi-element wavelength-dispersive
1051 spectroscopy (WDS) mapping of sharp contact between orthopyroxene-rich and
1052 metasomatised portion of Cu-rich pyroxenite sample.
1053
1054 Fig. 8. (a) Fluid inclusions in the cloudy clinopyroxene of sample X05. In the zoomed area, the
1055 fluid inclusions appear in healed fractures and along the cleavage planes of the clinopyroxene.
1056 The white arrow shows a whisker, suggesting decrepitation of the FI. Abbreviations: L - liquid

1057 phase; V - vapor phase. (b) Main Raman bands of the components (CH_4 and H_2) of the FIs.
1058 The stars note the Raman bands of the host clinopyroxene.

1059

1060 Fig. 9. Concordia plots of titanite U–Pb isotopic results

1061

1062 Fig. 10. Variations of $\delta^{65}Cu$ values in the Cheshmeh-Bid Cu-rich pyroxenites. Data of
1063 peridotites from previous studies are also shown for comparison. The grey rectangle represents
1064 the estimated $\delta^{65}Cu$ value of the Bulk Silicate Earth (BSE: 0.07±0.10‰, Savage et al., 2015).

1065

1066 Fig. 11. Isocon diagram for major (a), and trace and rare earth elements (b) using the method
1067 of Grant (2005) comparing average composition of Cheshmeh-Bid fresh orthopyroxenites and
1068 average composition of five metasomatised samples. The error bars correspond to +/- one
1069 standard deviation. Scaling factors have been used to display a better dispersion of the
1070 elements. Scaling factors are shown on isocon diagrams. The lines for constant total mass
1071 (black dashed line), constant total volume (black dotted line) and the best fit of the composition
1072 in immobile elements (isocon assuming Sc and TiO_2 as immobile; black plain line) are
1073 displayed. No change in composition is assumed along the isocon. The grey dashed lines
1074 correspond to compositions calculated for different mass gain(+)/loss(-). The densities used for
1075 constant volume and volume change calculations are 2896 kg/m^3 for the fresh orthopyroxenites
1076 and 3870 kg/m^3 for the Cu-bearing metasomatised samples. They are retrieved with image
1077 analysis of the modal composition in the fresh orthopyroxenite and in zone III. *: estimated
1078 based on image analysis.

1079

Fig. 12. Temperature-μCaO pseudosection for the composition of sample IRKJPX20 (orthopyroxenite) at 50 MPa. μCaO calculated as a function of temperature is displayed for the orthopyroxenite and three samples affected by Ca-metasomatism (IRKJPX04, IRKJPX11 and IRKJPX12). Tlc: talc; Atg: antigorite; Amp: amphibole; Cpx: clinopyroxene; Chl: chlorite; Ol: olivine; Brc: brucite; Wo: wollastonite; Mont: monticellite; Ves: vesuvianite; Rnk: rankinite.

Fig. 13. Sulfide and oxide stabilities as a function of $a_{H2,aq}$ and $a_{H2S,aq}$ in the Cu-Fe-Ni-O-S system. The phase diagrams are computed at 50 MPa, a_{H2O} = 1 and 200°C (a), 300°C (b) and 400°C (c). The boundaries in the Fe-O-S, Cu-O-S, Fe-Ni-O-S,, and Cu-Fe-O-S systems are displayed with grey dashed lines, green plain lines, black plain lines and red plain lines, respectively. The blue spot corresponds to the intersection of the pentlandite/heazlewoodite and the chalcocite/Cu boundaries. This intersection is used to determine the stability of native copper in a system where $a_{H2,aq}$ and $a_{H2S,aq}$ are buffered by the pentlandite/heazlewoodite equilibrium.

Fig. 14. a_{H2} as a function of temperature for the $H_{2,aq} = H_{2,g}$ equilibrium (black line) and the 2 Pentlandite + 12 H_2O + 20 Native Copper = 3 Heazlewoodite + 3 Magnetite + 10 Chalcocite + 12 $H_{2,aq}$ equilibrium (red line). This latter equilibrium allows to determine the activity in hydrogen at which the transition from chalcocite to native copper occurs in the rock. Hydrogen partial pressure and hydrostatic pressure are assumed to be equal (50 MPa).

Fig. 15. Schematic model for the genesis of Cu-rich pyroxenite from the Cheshmeh-Bid massif. Figures (a) and (b) are presented as meso-scale.

Supplementary Figure Captions

Supplementary Fig. 1. Pyroxene ternary diagram showing clino- and orthopyroxene compositions from the Cheshmeh-Bid Cu-rich pyroxenites.

Supplementary Fig. 2. Plot of the analysed chlorites on their classification diagram (after Hey, 1954).

Supplementary Fig. 3. Modes (vol.%) of the phases as a function of temperature and chemical potential in CaO for the pseudosection calculated with the composition of sample IRKJPX20 at 50 MPa. (a) Olivine. (b) Antigorite. (c) Clinopyroxene. (d) Amphibole.

Supplementary Table Captions

Table S1. Representative analyses of orthopyroxenes from the Cheshmeh-Bid Cu-bearing pyroxenites

Table S2. Representative analyses of olivine with vein-like texture from the Cu-bearing pyroxenites

Table S3. Representative analyses of chromian spinels in the Cheshmeh-Bid Cu-bearing pyroxenite

Table S4. Representative analyses of amphiboles from the Cheshmeh-Bid Cu-bearing pyroxenites

Table S5. Representative analyses of clinopyroxenes from the Cheshmeh-Bid Cu-bearing pyroxenites

Table S6. Representative analyses of chlorites in Zone III from the Cu-bearing pyroxenites

Table S7. Chemical compositions of sulfides in Zone III

Table S8. Composition of the fluid phase (liquid+vapor) in studied clinopyroxene-hosted fluid inclusions from the PX05 sample.

Table S9. Laser ablation ICP-MS U-Pb analyses including U and Pb contents, isotopic ratios and ages of seven titanite grains from the Cheshmeh-Bid Cu-bearing pyroxenites

Table S10. Copper isotopic results of eight native copper grains from the Cheshmeh-Bid Cu-bearing pyroxenite

Table S11. Whole-rock analyses of the Cheshmeh-Bid pyroxenites.

1155 Figure 1

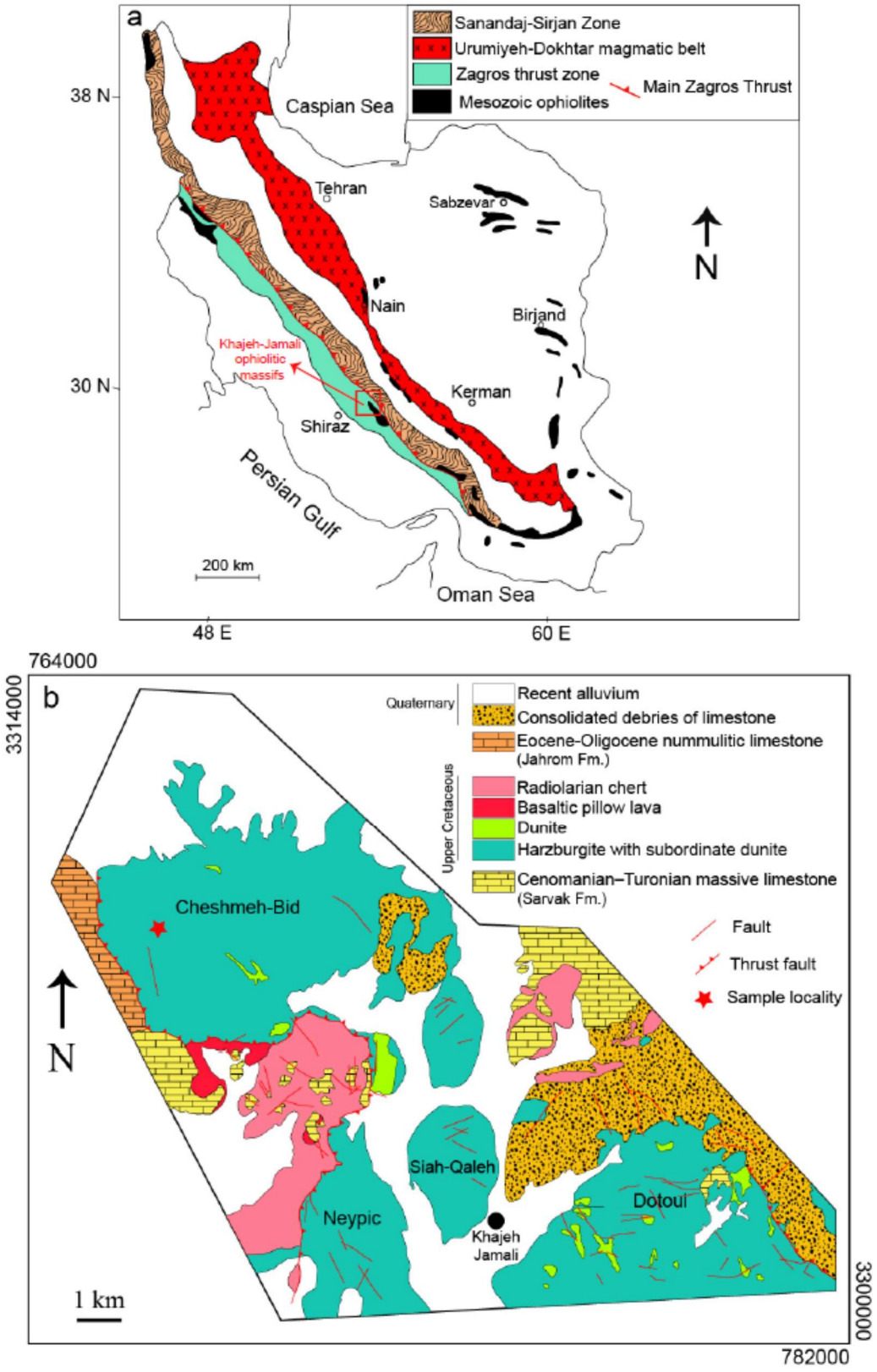

1156

1157

1158

Figure 2

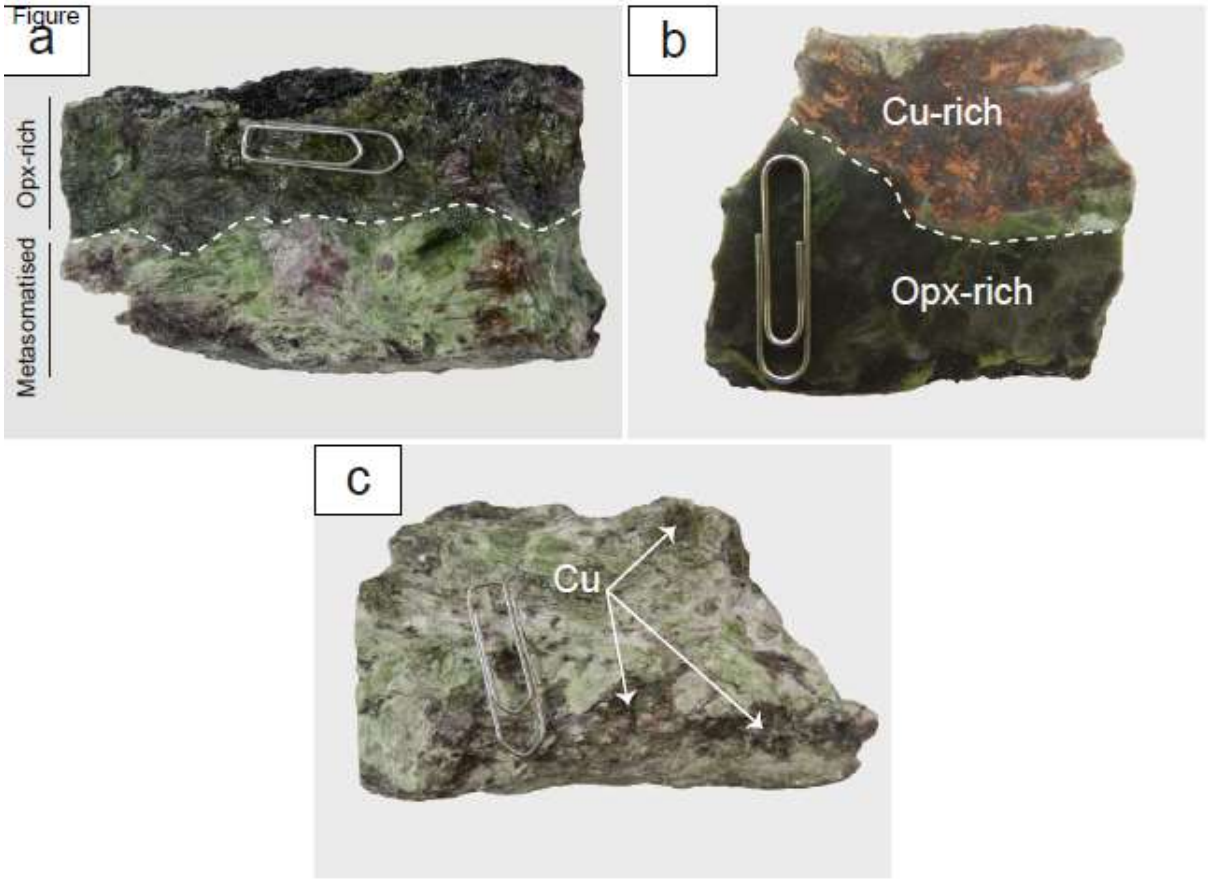

1173 Figure 3

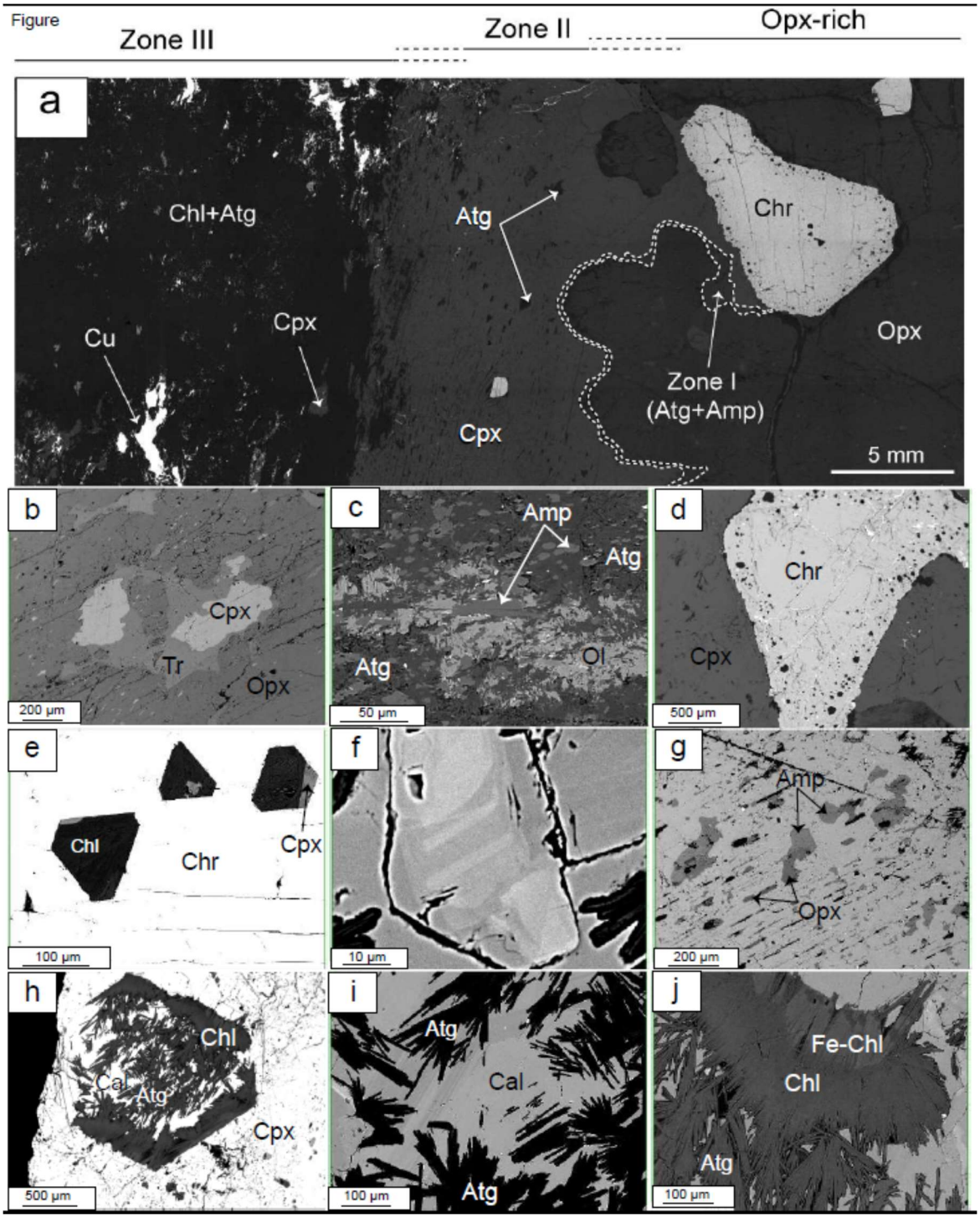

1174

1175

1176

1177

1178

Figure 4

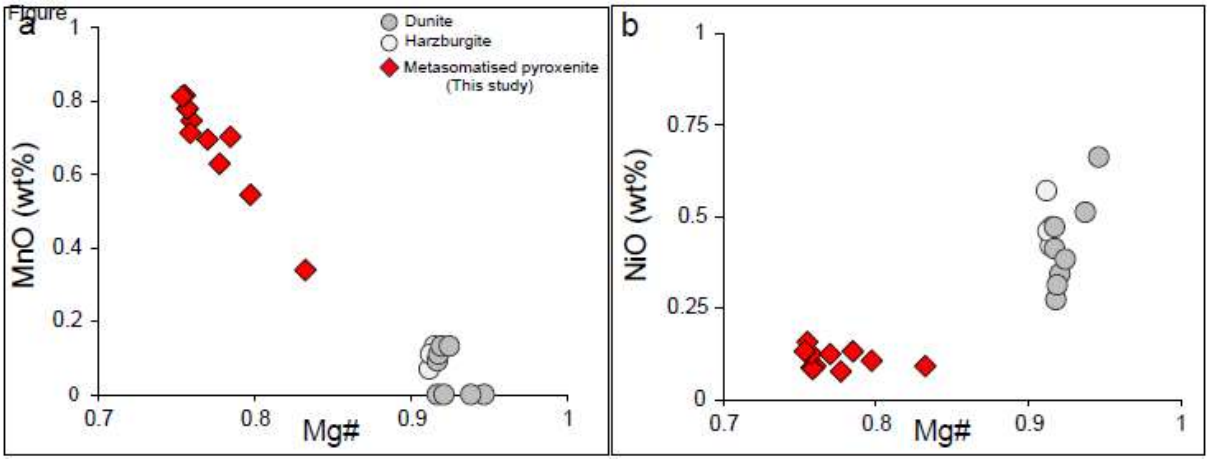
Figure
a
Dunite
Harzburgite
Metasomatised pyroxenite
(This study)
MnO (wt%)
Mg#
b
NiO (wt%)
Mg#

1199 Figure 5

Figure

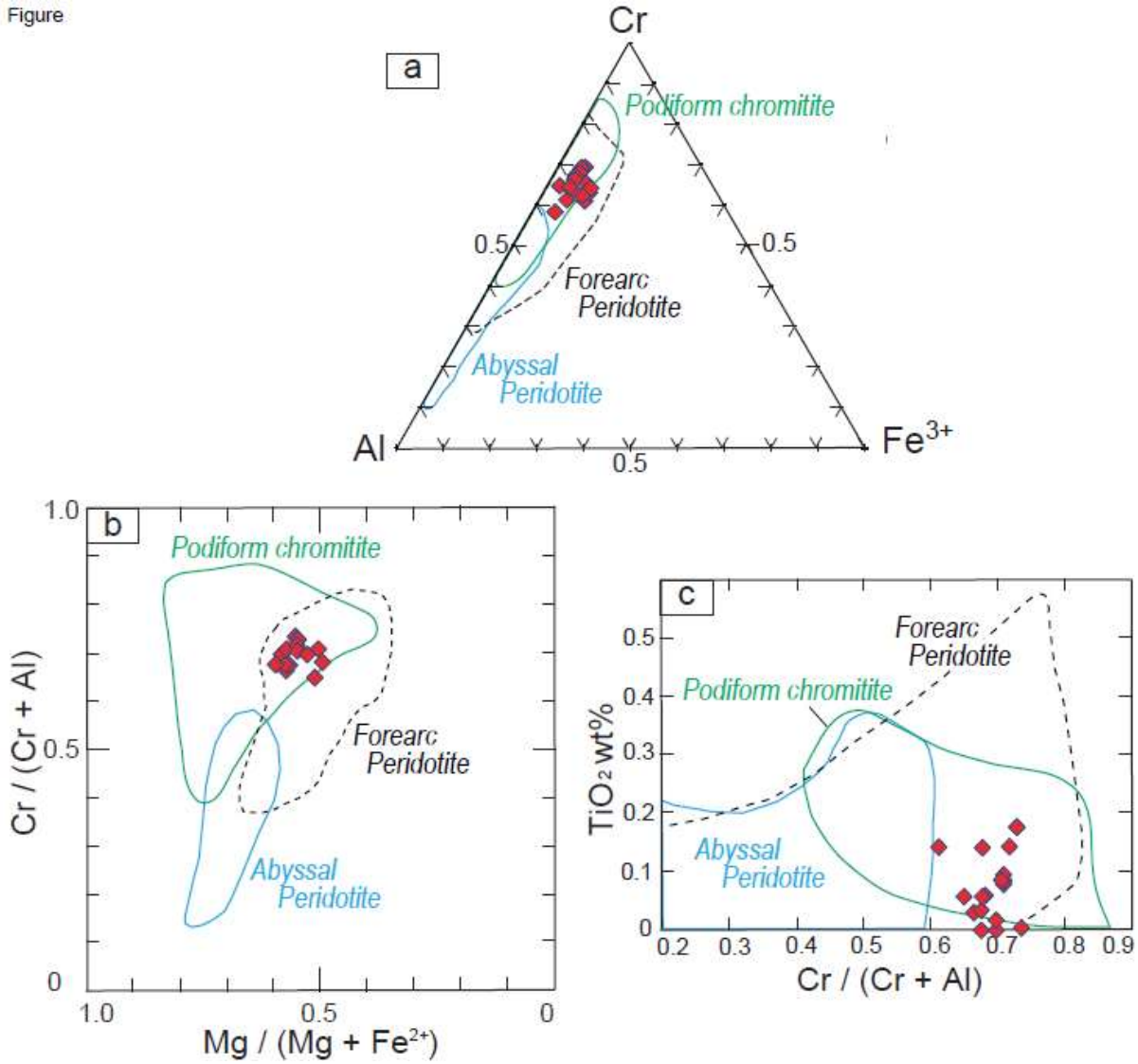

1200

1201

1202

1203

1204

1205

1206

1207

1208

1209

Figure 6

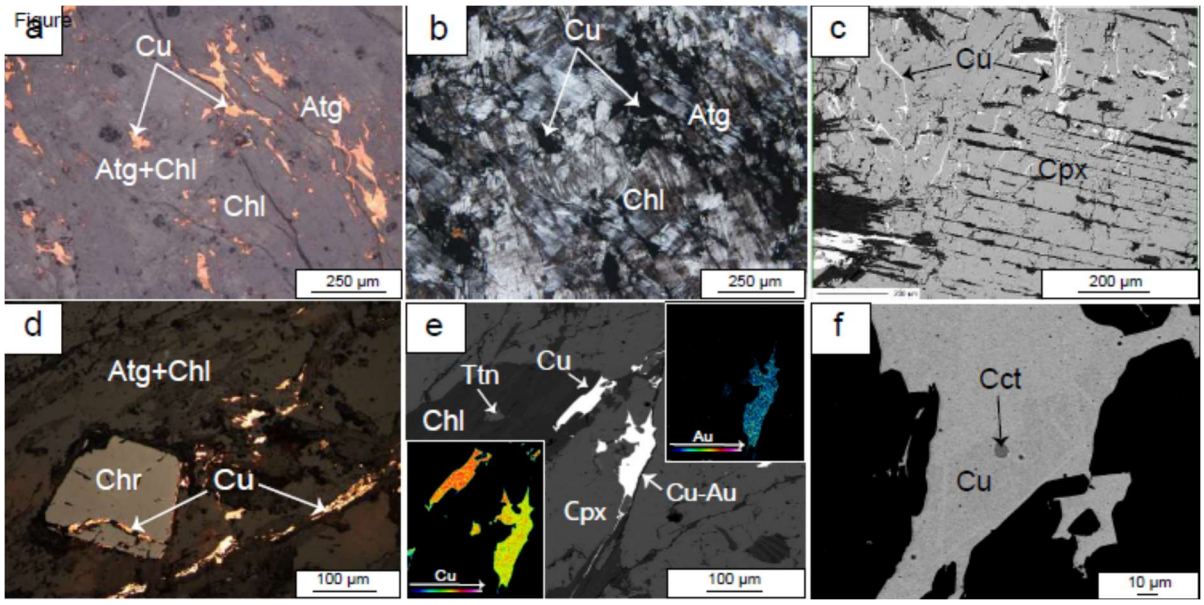
a
Cu
Atg
Atg+Chl
Chl
250 µm
b
Cu
Atg
Chl
250 µm
c
Cu
Cpx
200 µm
d
Atg+Chl
Chr
Cu
100 µm
e
Ttn
Cu
Chl
Au
Cu
Cpx
Cu-Au
100 µm
f
Cct
Cu
10 µm

Figure 7

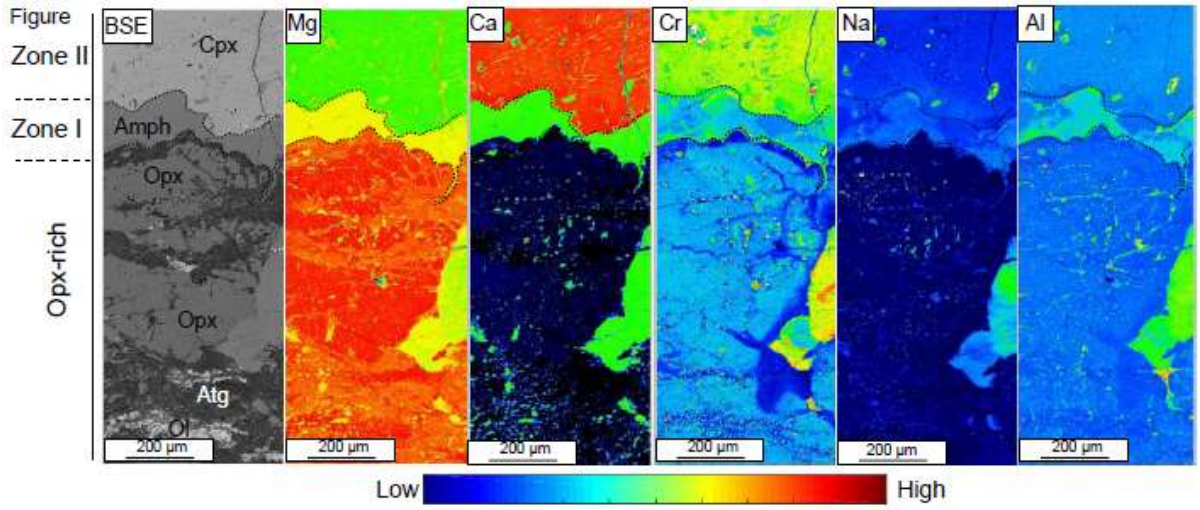
Figure
Zone II
Zone I
Opx-rich
BSE
Cpx
Amph
Opx
Opx
Atg
Mg
Ca
Cr
Na
Al
200 µm
Low
High

Figure 8

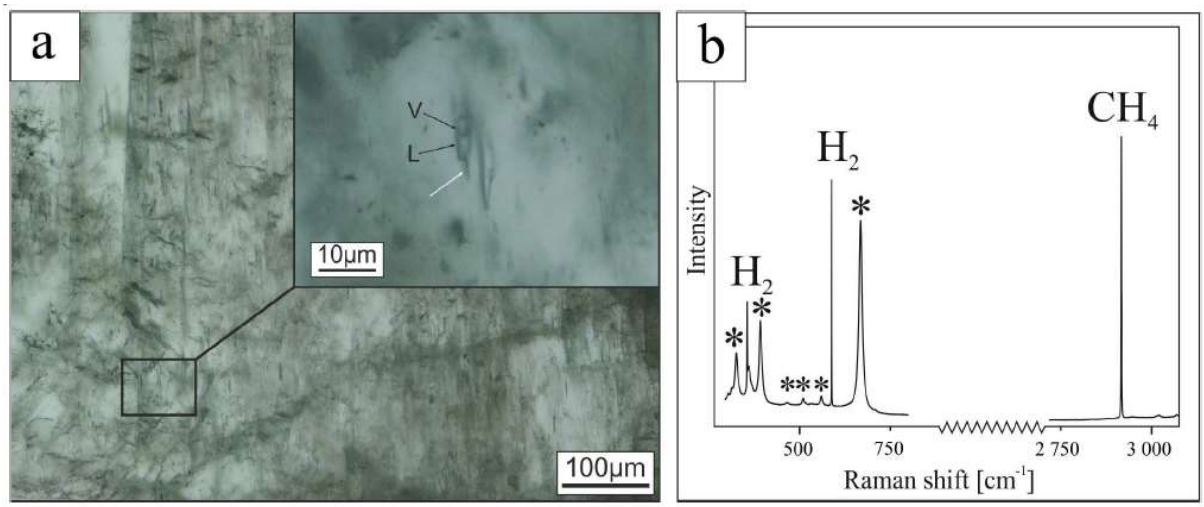
a
V
L
10μm
100μm
b
CH4
H2
H2
Intensity
500
750
2 750
3 000
Raman shift [cm-1]

Figure 9

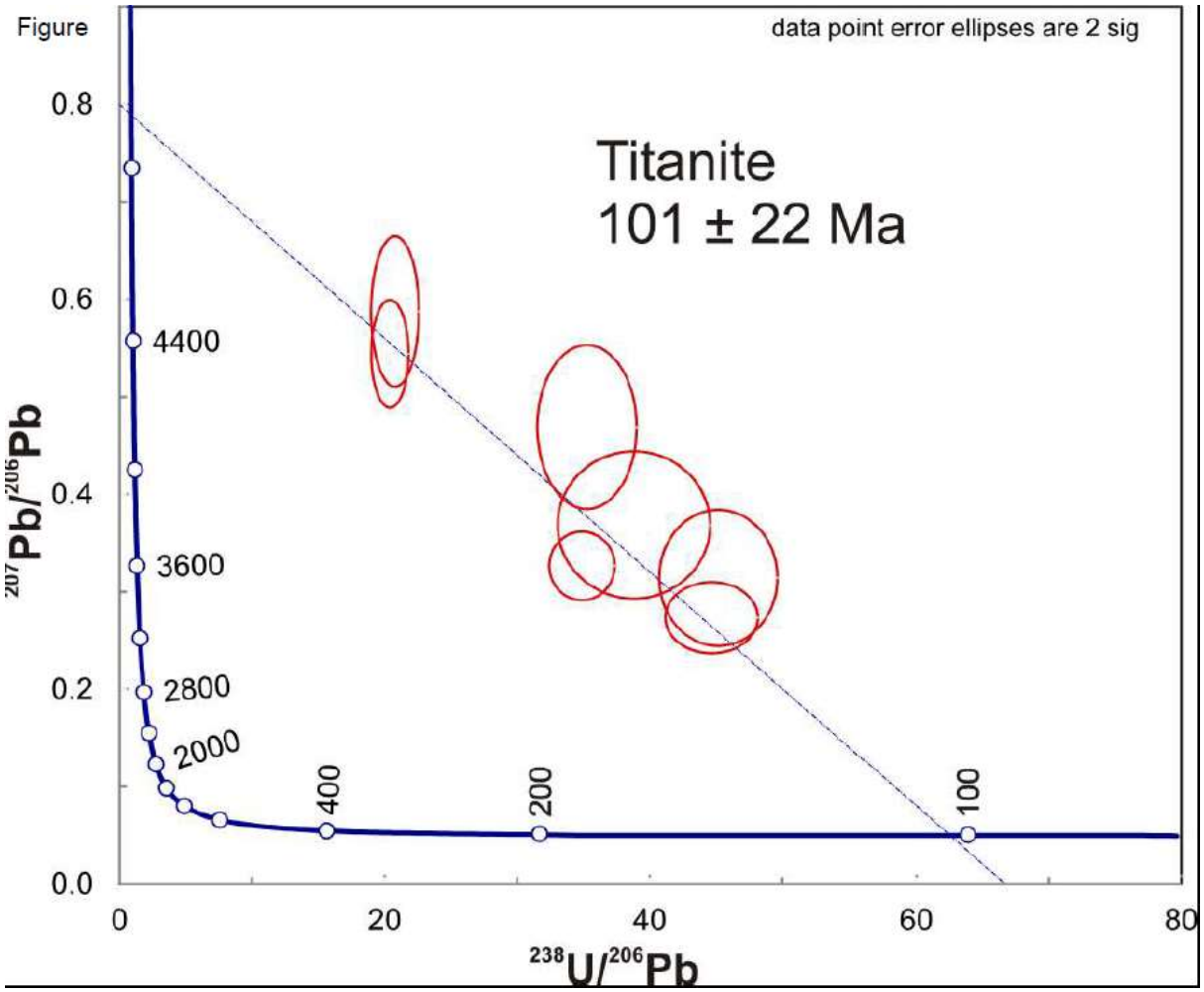
Figure
data point error ellipses are 2 sig
Titanite
101 ± 22 Ma
0.8
0.6
0.4
0.2
0.0
4400
3600
2800
2000
400
200
100
0
20
40
60
80
$^{207}Pb/^{206}Pb$
$^{238}U/^{206}Pb$

Figure 10

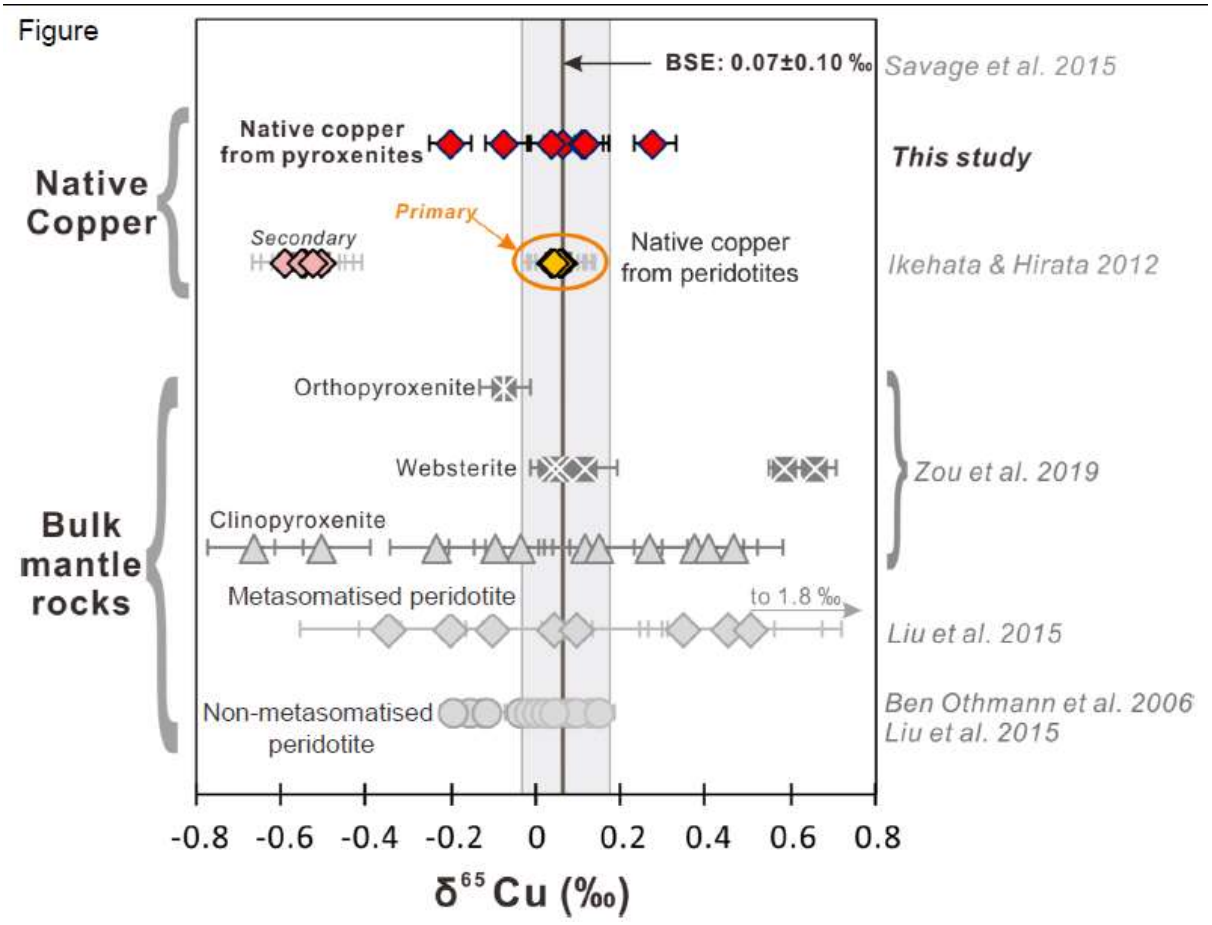
Figure
BSE: 0.07±0.10 ‰
Savage et al. 2015
Native copper from pyroxenites
This study
Native Copper
Primary
Secondary
Native copper from peridotites
Ikehata & Hirata 2012
Orthopyroxenite
Websterite
Zou et al. 2019
Bulk mantle rocks
Clinopyroxenite
Metasomatised peridotite
to 1.8 ‰
Liu et al. 2015
Non-metasomatised peridotite
Ben Othmann et al. 2006
Liu et al. 2015
-0.8 -0.6 -0.4 -0.2 0 0.2 0.4 0.6 0.8
δ65 Cu (‰)

Figure 11

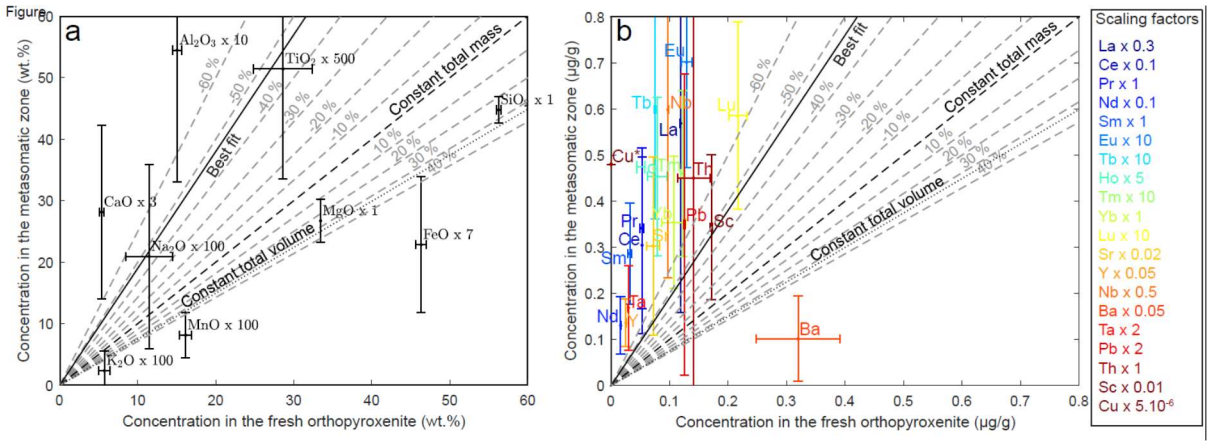
a
b
Concentration in the metasomatic zone (wt.%)
Concentration in the fresh orthopyroxenite (wt.%)
Concentration in the metasomatic zone (µg/g)
Concentration in the fresh orthopyroxenite (µg/g)
Best fit
Constant total mass
Constant total volume
Al2O3 x 10
TiO2 x 500
TiO2 x 1
CaO x 3
MgO x 1
FeO x 7
Na2O x 100
MnO x 100
K2O x 100
Scaling factors
La x 0.3
Ce x 0.1
Pr x 1
Nd x 0.1
Sm x 1
Eu x 10
Tb x 10
Ho x 5
Tm x 10
Yb x 1
Lu x 10
Sr x 0.02
Y x 0.05
Nb x 0.5
Ba x 0.05
Ta x 2
Pb x 2
Th x 1
Sc x 0.01
Cu x 5.10-6

Figure 12

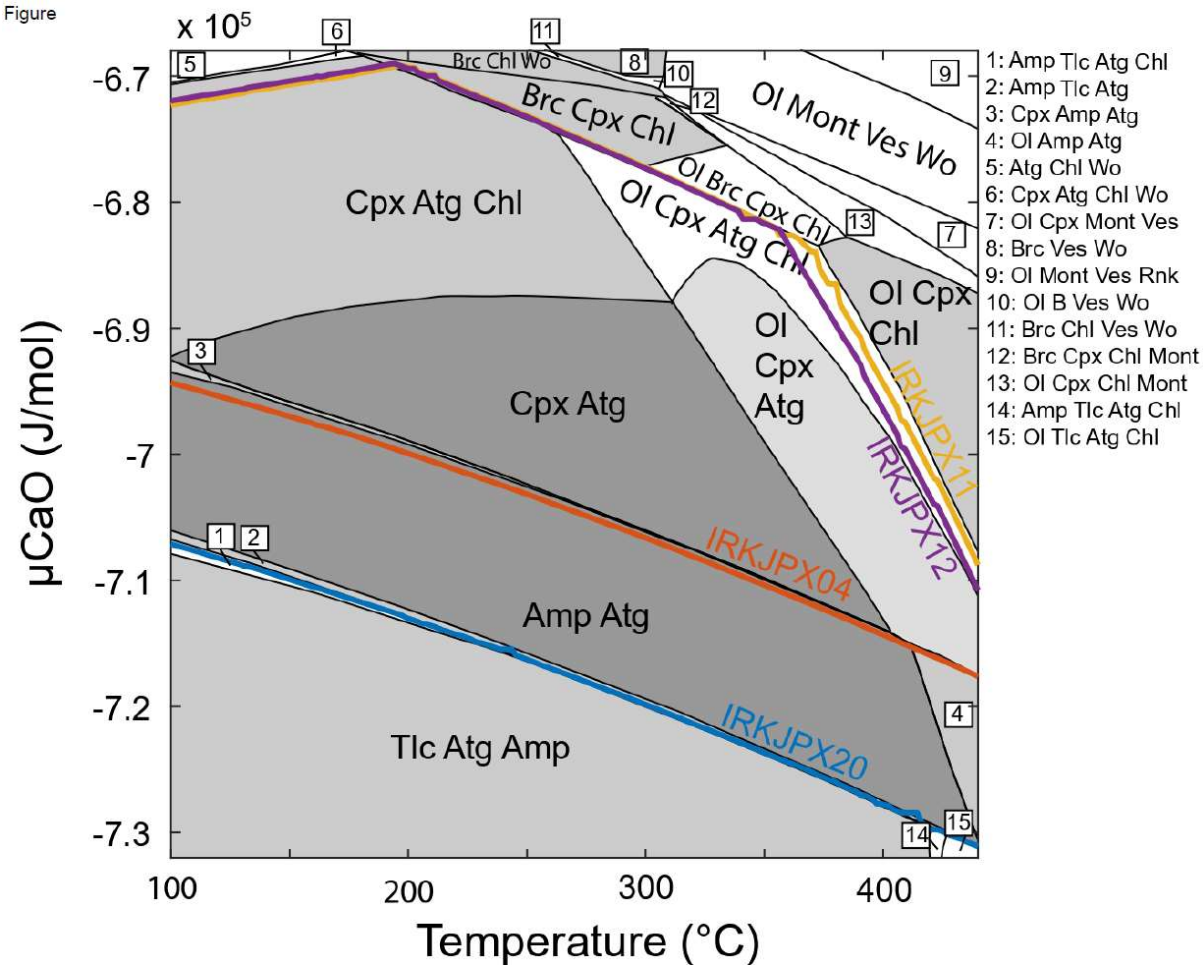
Figure
x 10^5
-6.7
-6.8
-6.9
-7
-7.1
-7.2
-7.3
μCaO (J/mol)
100
200
300
400
Temperature (°C)
Brc Chl Wo
Brc Cpx Chl
Ol Mont Ves Wo
Ol Brc Cpx Chl
Ol Cpx Atg Chl
Cpx Atg Chl
Ol Cpx Chl
Ol Cpx Atg
Cpx Atg
Amp Atg
Tlc Atg Amp
IRKJPX11
IRKJPX12
IRKJPX04
IRKJPX20
1: Amp Tlc Atg Chl
2: Amp Tlc Atg
3: Cpx Amp Atg
4: Ol Amp Atg
5: Atg Chl Wo
6: Cpx Atg Chl Wo
7: Ol Cpx Mont Ves
8: Brc Ves Wo
9: Ol Mont Ves Rnk
10: Ol B Ves Wo
11: Brc Chl Ves Wo
12: Brc Cpx Chl Mont
13: Ol Cpx Chl Mont
14: Amp Tlc Atg Chl
15: Ol Tlc Atg Chl

1324 Figure 13

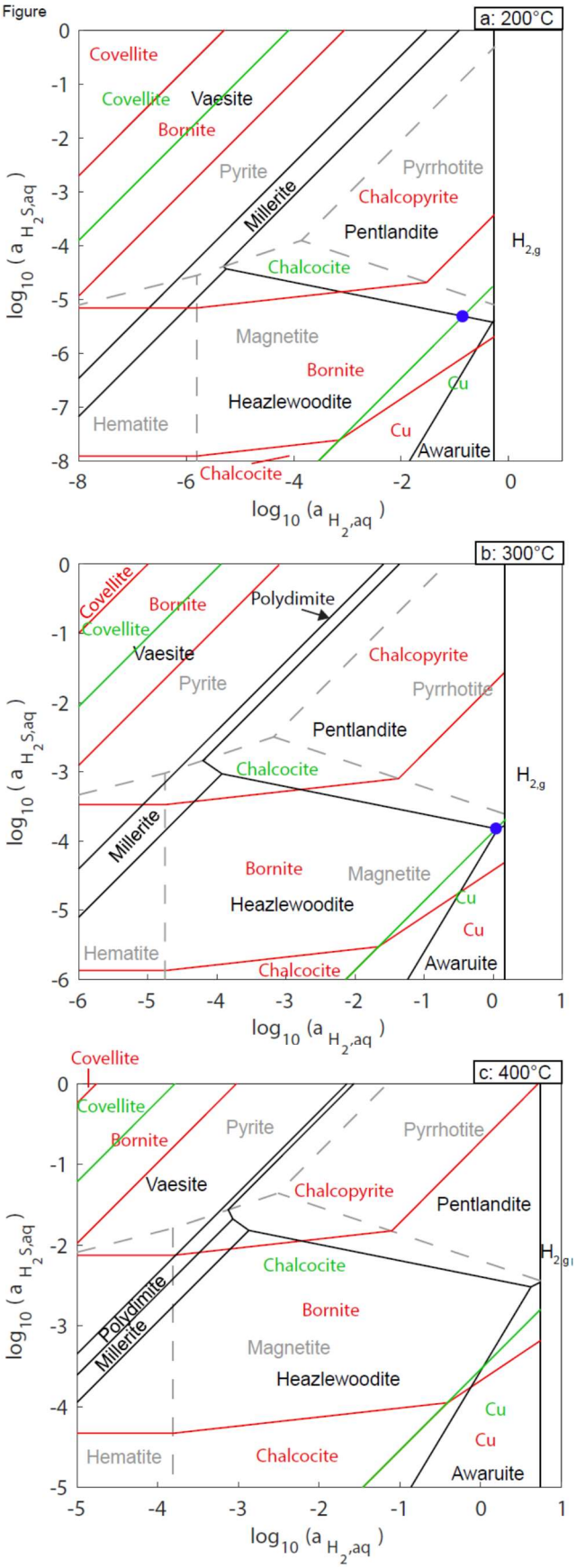

1325

Figure 14

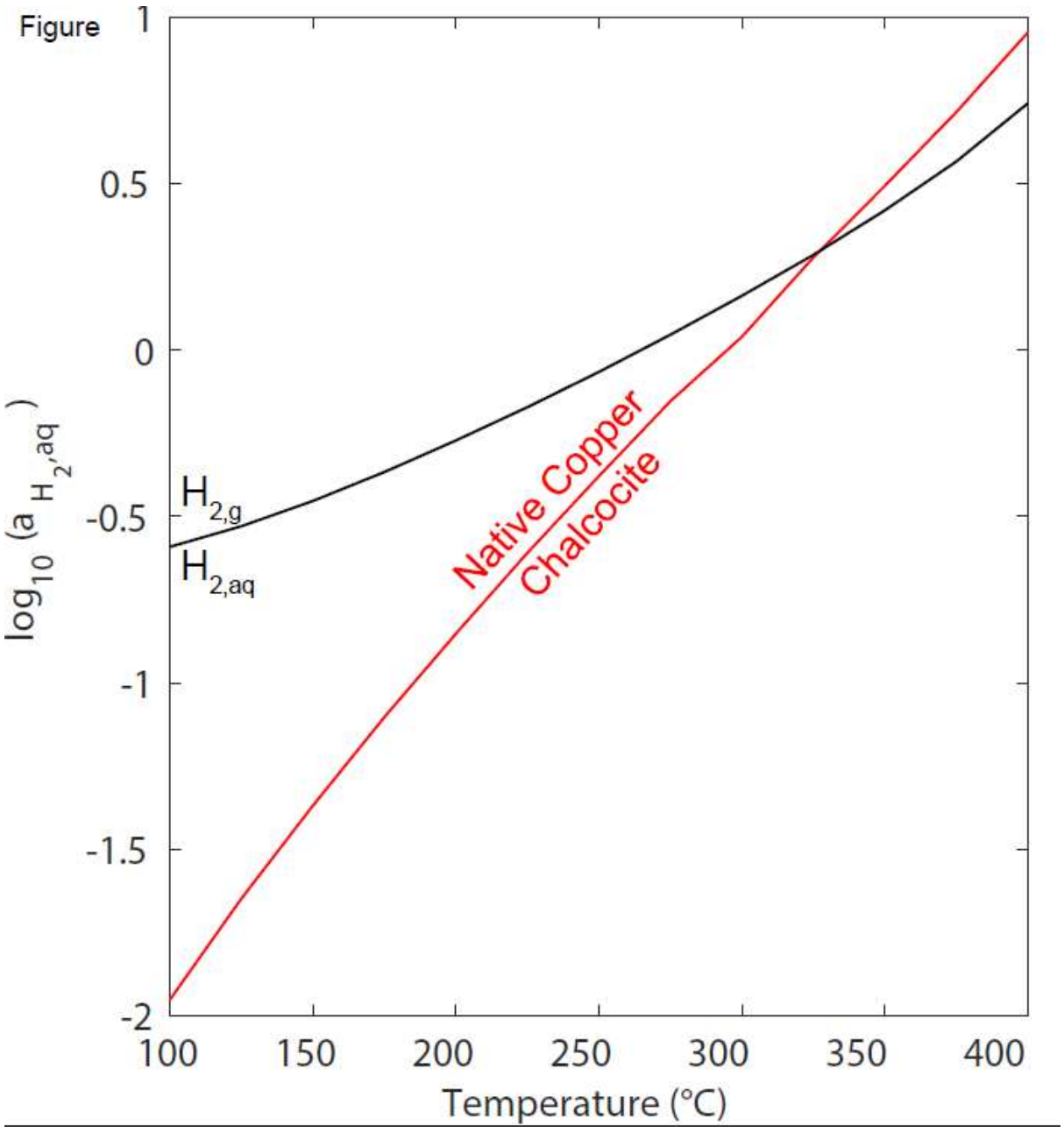
Figure
1
0.5
0
-0.5
-1
-1.5
-2
100
150
200
250
300
350
400
Temperature (°C)
log10 (a H2,aq)
H2,g
H2,aq
Native Copper
Chalcocite

1334 Figure 15

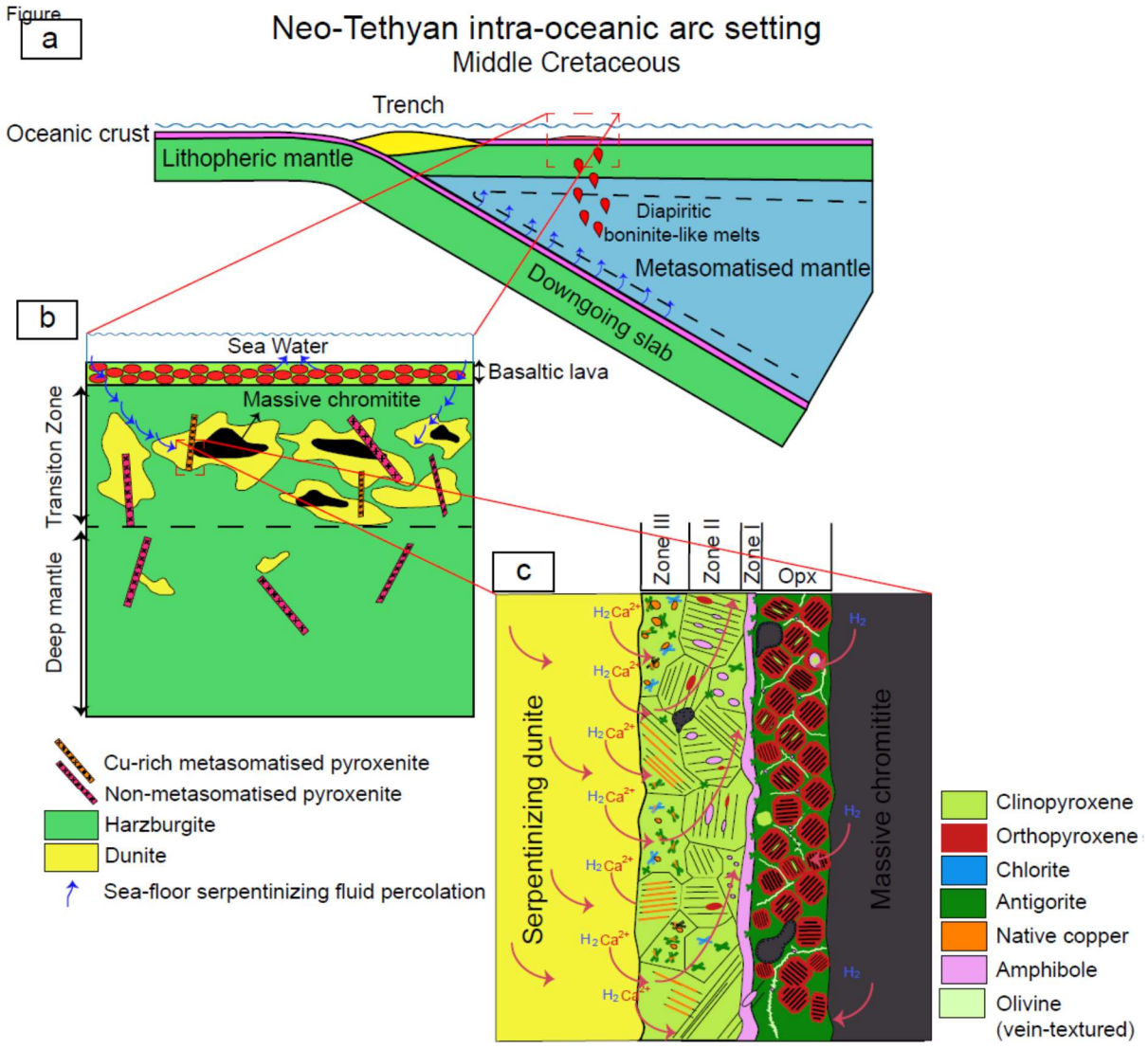

1335

1336